In operando neutron diffraction study of $LaNdMgNi_9$ as a metal hydride battery anode

N. S. Nazer[1, 2], R.V. Denys[1], V.A. Yartys[1, 2 *], Wei-Kang Hu[1], M.Latroche[3], F.Cuevas[3], B.C. Hauback[1], P.F.Henry[4] and L. Arnberg[2]

(1) Institute for Energy Technology, Kjeller, NO-2027, Norway;
(2) Norwegian University of Science and Technology, Trondheim, NO-7491, Norway;
(3) Université Paris Est, ICMPE (UMR7182), CNRS, UPEC, F-94320 Thiais, France;
(4) European Spallation Source ERIC, Lund, S-221 00, Sweden

ABSTRACT

La_2MgNi_9-related alloys are superior metal hydride battery anodes as compared to the commercial AB_5 alloys. Nd-substituted $La_{2-y}Nd_yMgNi_9$ intermetallics are of particular interest because of increased diffusion rate of hydrogen and thus improved performance at high discharge currents. The present work presents *in operando* characterization of the $LaNdMgNi_9$ intermetallic as anode for the nickel metal hydride (Ni-*M*H) battery. We have studied the structural evolution of $LaNdMgNi_9$ during its charge and discharge using *in situ* neutron powder diffraction. The work included experiments using deuterium gas and electrochemical charge-discharge measurements. The alloy exhibited a high electrochemical discharge capacity (373 mAh/g) which is 20 % higher than the AB_5 type alloys. A saturated β-deuteride synthesized by solid-gas reaction at P_{D2} = 1.6 MPa contained 12.9 deuterium atoms per formula unit (D/f.u.) which resulted in a volume expansion of 26.1%. During the electrochemical charging, the volume expansion (23.4%) and D-contents were found to be slightly reduced. The reversible electrochemical cycling is performed through the formation of a two-phase mixture of the α-solid solution and β-hydride phases. Nd substitution contributes to the high-rate dischargeability, while maintaining a good cyclic stability. Electrochemical Impedance Spectroscopy (EIS) experiments showed a decreased hydrogen transport rate during long-term cycling.

Keywords:

- Metal hydride
- In situ neutron diffraction
- Electrochemical Impedance Spectroscopy
- Neodymium
- Magnesium
- Lanthanum

*) Corresponding author. E-mail: volodymyr.yartys@ife.no.

1. INTRODUCTION

Rechargeable batteries should provide high energy density, safety, environmental compatibility, low cost, long calendar life, small size and light weight, with properties tailored towards the demand required from applications. Aiming at satisfying these requirements, nickel-metal hydride (Ni-*M*H) batteries, belonging to the green batteries, have been developed and commercialized [1, 2]. In the Ni-*M*H batteries, hydrogen storage alloys (their hydrides) are used as active materials immersed into an aqueous alkaline electrolyte (KOH). $LaNi_5$ was the first anode material used in the *M*H battery. However, its rapid capacity decay on cycling limited its commercial application [3]. This drawback was addressed by modifying $LaNi_5$ via a substitution of Ni by Co and Al and of La by a mischmetal [4]. Thus, a rapid market growth of the Ni-*M*H batteries took place and they became the dominant advanced battery technology for hybrid electric vehicles (HEVs) fulfilling the requirements set by automotive companies [5].

A variety of hydrogen storage alloys have been studied, including the rare earth based AB_5-type alloys, Ti and Zr based AB_2 alloys, *AB*, Mg-based and the Rare Earth (*RE*)-Mg-Ni based alloys as active anode materials [6, 7]. The latter alloys include a series of ternary rare earth magnesium based hydrogen storage alloys with a stoichiometric composition RE_2MgNi_9 (where, *RE*=La) reported back in 2000 [8]. Development of the Mg-containing alloys allowed increasing electrochemical discharge capacity, from 320 mAh/g (AB_5) to 400 mAh/g, for the Mg-containing alloys.

Recently, systematic theoretical and experimental studies of the La–Mg–Ni-based hydrogen storage alloys with super-stacking structures have been performed [9], as they are regarded as high performance negative electrode materials of the Ni-*M*H batteries. Liao *et al.* [10] reported that electrochemical discharge capacity of the La_2MgNi_9 electrode of 397 mAh/g. Modelling of the electrochemical discharge process of the metal hydride electrode [9], allowed an optimization of the metal hydride electrodes, based on estimation of the diffusion coefficient of hydrogen and equilibrium content of H in the solid solution domain in the metal hydrides.

Ternary La-Mg-Ni intermetallics include three different stoichiometric ratios between *A*-elements (*A* = Mg and Rare Earths *RE*) and *B*-elements (*B* = Ni), AB_3, A_2B_7 and A_5B_{19}, which all show a good performance as battery anodes in the high energy/high power Ni-*M*H batteries [11, 12]. These compounds belong to the hybrid AB_x layered structures, where individual Laves type AB_2 layer, $La_{2-y}Mg_yNi_4$, and Haucke type AB_5 layers, $LaNi_5$, stack along the hexagonal/trigonal axis in different ratios ($AB_3 = AB_5 + 2\ AB_2$; $A_2B_7 = AB_5 + AB_2$; $A_5B_{19} = 3\ AB_5 + 2\ AB_2$).

A detailed review on the structural, thermodynamic and electrochemical properties of the metallic hydrides belonging to the pseudo-binary family *RE*–Mg–Ni has been published recently [13]. Improving the hydrogen storage properties of La–Mg–Ni-based alloys by such methods as elemental substitution in the alloy composition [12, 14-16], rapid quenching [17], composite alloying (by Mn, Al) and surface modification [18] have been employed by several groups.

Among these methods elemental substitution was found to be the most efficient way to improve the cycling stability of La–Mg–Ni-based alloys.

Hydrogen absorption–desorption behaviours, electrochemical performance and cycling stability of La_2MgNi_9 alloy can be significantly improved by annealing [19]. *In-situ* neutron diffraction has been utilized to study the mechanism and kinetics of the temperature-induced phase-structural transformations in La_2MgNi_9 [20]. Interactions of La–Mg–Ni alloys with hydrogen were also studied by *in-situ* synchrotron X-ray and neutron powder diffraction [21]. $LaNi_5$ and $LaMgNi_4$ layers were found to be occupied by D atoms to form $LaNi_5D_{5.2}$ and $LaMgNi_4D_{7.9}$ compositions showing that the hydrogen to metal atomic ratio (H/M) varies between 0.87 ($LaNi_5$ layer) and 1.32 H/M ($LaMgNi_4$ layer). Four D-sites are located within the $LaMgNi_4$ slab, two within the $LaNi_5$ slabs and two sites are placed at a boundary between the slabs.

Partial substitution of La by Nd is considered as an effective way to improve the electrochemical properties of La–Mg–Ni-based alloys [22]. Studies revealed that Nd has a positive influence on several features; (a) it improves the resistance to oxidation; (b) it increases the exchange current at the surface of the anode electrode; (c) it increases the rate of the bulk diffusion of hydrogen atoms in the $(La,Ce,Pr,Nd)_2MgNi_9$ alloy. As a consequence, these three features contribute together to enhance the cycle life and high rate dischargeability of the anodes. Most of the studies put an emphasis on investigating the effects of the different ratio between La substitutions by Nd on the electrochemical properties of La–Mg–Ni-based alloys [23-27].

In general, chemical compositions of the studied alloys and their crystal structures can be separated into (a) AB_3 alloys with $PuNi_3$ type of structures; (b) A_2B_7 with Ce_2Ni_7 type of structures. The general regularities of their interaction with hydrogen and properties of the metal hydrides have many common features. Recently, our group [28] found that with a partial substitution of Nd for La, the formed $La_{1.5}Nd_{0.5}MgNi_9$ alloy was composed of $PuNi_3$-type phase only, and showed improvement in the cycling stability and high rate dischargeability. Changes in hydrogen diffusion rate in the $La_{1.5}Nd_{0.5}MgNi_9$ anode appeared to be related to the changes in hydrogen content [29]. The diffusion coefficient reached a maximum at 85% of discharge.

The overall focus of our work is on the AB_3 type alloys based on La, Mg and Ni. La substitution for Nd and Pr is as a part of the strategy to achieve the best high rate performance of the battery anodes at optimized content of the constituents. Here, neutron scattering on deuterated samples provides important information on the mechanism and kinetics of phase-structural transformations as related to their performance of hydrogen storage materials and battery anodes.

Earlier we have performed *in situ* NPD experiments on the lanthanum-based systems, $La_{3-x}Mg_xNi_9$-D_2. The alloys with a variable Mg content were studied by monitoring solid-D_2 gas interactions and during electrochemical charge-discharge of the metal hydride anode electrodes [21, 30, 31]. Study of $La_2MgNi_9D_{13}$ revealed a novel type of the metal-hydrogen ordering built

by a stacking of the MgH_6 and NiH_4 polyhedra [32], while $LaNi_5$-assisted hydrogenation of $MgNi_2$ has been observed in the structure of $LaMg_2Ni_9$ at pressures up to 100 MPa D_2 [33].

In contrast, much less is known on the structural and hydrogen sorption properties of the compounds containing other light rare-earth metals, mainly Pr and Nd. However, these alloys could be very important as electrode materials because of a much increased mobility of hydrogen in the Nd based hydrides [34]. A partial substitution of La by Pr/Nd is expected to improve their cyclic stability and high-rate dischargeability [22, 34]. Thus, replacement of La by other *RE* together with optimization of Mg content [31] provides complementary possibilities to improve the alloys. Nd-doped La_2MgNi_9 showed a better performance at high current densities [13, 28].

Table 1 summaries the available data on structure and on the thermodynamics and electrochemistry of the metal hydrides formed by three intermetallic with RE_2MgNi_9 composition, which were characterized in our earlier studies [28], including La_2MgNi_9, $La_{1.5}Nd_{0.5}MgNi_9$ and Nd_2MgNi_9.

Table 1. Crystallographic, thermodynamic and electrochemical data for the $(La,Nd)_2MgNi_9$ systems

Alloy	Unit cell dimensions	H storage capacity, wt.% H	Plateau pressure, MPa (293 K)	ΔH (kJ/mol H_2) and ΔS (J/Kmol H_2)	Discharge capacity, mAh/g at *C*/10	Ref.
La_2MgNi_9	a = 5.0314 Å c = 24.302 Å V = 532.79 Å^3	1.5	0.005	ΔH = 35.9, ΔS = 96.7	375	[31]
$La_{1.5}Nd_{0.5}MgNi_9$	a = 5.0258 Å c = 24.305 Å V = 531.66 Å^3	1.4	0.01	-	410	[28]
Nd_2MgNi_9	a = 4.9783Å c = 24.1865Å V = 519.12 Å^3	1.46	0.14	ΔH = 28.6, ΔS = 99.5	-	[34]

Earlier, phase-structural transformations in an Mg-and Nd-modified $LaNi_3$ intermetallic have been studied by NPD experiments [28, 29, 35]. Although the work on $La_{1.5}Nd_{0.5}MgNi_9$ showed that Nd substitution for La can significantly improve the electrochemical properties of the alloys, it is essential to make a more comprehensive investigation of the impact of Nd substitution for La on the crystal structure and phase transformation of the alloys by systematically studying the materials with a variable Nd content and La/Nd ratios.

The objective of the present work was to conduct a detailed study of intermetallic alloy containing equal amounts of La and Nd while keeping Mg content at an optimum level (1 Mg / 2 *RE*) thus arriving to the composition $LaNdMgNi_9$. The focus was to reveal the structural evolution of $LaNdMgNi_9$ during cycling by means of *in situ* and *in operando* neutron powder diffraction both for the metal-gas interactions and for the electrochemical charge-discharge of the metal hydride anode and on studying the dependence of the electrochemical performance of the

$(La_{2-y}Nd_y)MgNi_9$ alloys on Nd-content, when comparing $LaNdMgNi_9$ with earlier studied La_2MgNi_9 [31] and $La_{1.5}Nd_{0.5}MgNi_9$ [28] counterparts.

2. EXPERIMENTAL METHODS

$LaNdMgNi_9$ was synthesized from arc melted pre-alloy $LaNdNi_9$ and fine Mg powder. $LaNdNi_9$ pre-alloy was prepared by arc melting in purified argon gas using individual metals (La, Nd, and Ni) with purity not less than 99.9 %. The as cast alloy was manually crushed into a fine powder (<60 µm; agate mortar) and mixed with a fine Mg powder (325 mesh, 99.8%). Mg was added in a slight excess (4 wt. %) in order to compensate for its losses during the sample preparation at high temperatures. In order to get a homogeneous distribution of the components, the powder mixture was ball milled in Ar atmosphere at 150 rpm for 1 h (Fritsch P6; 80 ml vial; balls/powder ratio = 10:1). Milled powder was pressed into the pellets (diameter 10 mm; applied pressure 12MPa). The pellets were loaded into a Ta foil and then placed into a stainless steel autoclave, filled with argon (0.08 MPa; room temperature) and sealed by welding. The autoclaves were heat treated at 950 °C for 10 h, followed by annealing at a lower temperature of 800 °C for 12 h. The autoclaves were quenched into cold water after the annealing.

Phase-structural analysis of the alloy was performed by X-ray powder diffraction using a Bruker D8 DISCOVER with a Ge-monochromator (Cu-Kα_1 radiation; λ = 1.5406 Å) and a LYNX-Eye detector. The experimental data was processed using Rietveld profile refinements and GSAS software [36, 37].

Hydrogen absorption–desorption properties of the alloy were characterized using a Sievert's apparatus. The sample was activated in vacuum at 250 °C for 30 min, cooled to 20 °C and then charged with a high purity hydrogen gas (99.999%). Pressure–composition–temperature (*PCT*) dependences of hydrogen absorption and desorption were measured on the activated samples at temperatures 20, 50 and 80 °C and at H_2 pressures from 10^{-4} to 2.5 MPa.

The deuteride for the NPD study was prepared by the following method: 5g of $LaNdMgNi_9$ alloy was ground into a coarse powder and loaded into a stainless steel sample holder (wall thickness 0.2 mm, d_{inner} = 6 mm) which was connected to a Sieverts' type apparatus and used as the sample cell during the NPD experiments. The sample was activated by a fast heating in dynamic vacuum to 250 °C followed by cooling it down to room temperature. Then, deuteration (D_2 gas, 99.8 % purity) of the sample was done overnight at room temperature at D_2 pressure of 1.6 MPa, until reaching a saturation of the sample by deuterium.

For the *in operando* NPD-electrochemical studies, the three-electrode system was prepared as described in reference [31]. The composite electrodes were made from 5g of intermetallic powder mixed with carbon black and PTFE in the weight ratio 90:5:5 and compressed over a nickel grid used as a current collector. The electrode was sandwiched between two counter-electrode cylinders made of nickel grid and immersed into a NaOD 5.5 M electrolyte solution. The potential was monitored against a solid Cd/Cd $(OH)_2$ reference electrode. The working

electrode was first charged in lab at a constant current rate of 0.1 *C*. Then, a galvanostatic discharge/charge cycle at C/20 rate (19 mA/g) was carried out with a cut-off potential of 0.5 V while neutron diffraction patterns were monitored. *In operando* neutron diffraction studies were performed at room temperature and ambient pressure using the High-Resolution Powder Diffractometer for Thermal Neutrons (HRPT- λ= 1.494 Å) in High Intensity mode at SINQ, PSI in Switzerland. Data acquisition and treatment are the same as described in reference [31].

Electrochemical properties were tested with a three electrode system at room temperature. The pelleted electrodes were prepared by mixing $LaNdMgNi_9$ alloy powder with carbonyl Ni powder. The mixture consisted of 20 wt. % of the alloy powder and 80 wt. % of carbonyl Ni powder. The pellet electrode of 10 mm diameter and thickness of approximately 1 mm was fabricated by cold pressing under a pressure of 12 MPa. Then the compressed pellet was sandwiched between two Ni foam sheets. Current density and cycling studies were tested in a three-electrode system with a 9 *M* KOH solution electrolyte at room temperature. A sintered $Ni(OH)_2$ electrode with a larger capacity than that of the *M*H electrode and an Hg/HgO electrode were used as the counter electrode and reference electrode, respectively. The charge/discharge tests were performed using a LAND CT2001A Battery Tester. The *M*H electrode was first activated at a current rate 100 mA/g for five charge–discharge cycles. Then, the rate capability, current density and cycling stability were evaluated galvanostatically at 300 mA/g.

Electrochemical impedance spectroscopy (EIS) measurements were performed using a Biologic SP-300 potentiostat in a frequency range of 100 kHz-0.5 mHz. The amplitude of perturbation to the electrodes was 10 mV. Cycling dependences of the impedance spectra of the electrodes were recorded after 20, 70, 150, 358 cycles at 50% DOD condition. The discharge state was obtained by discharging at 300 mA/g after reaching a full charge. The impedance spectra were fitted to an equivalent circuit using EC Lab software.

3. RESULTS AND DISCUSSION

3.1 X-ray diffraction study of $LaNdMgNi_9$

The XRD pattern of the $LaNdMgNi_9$ alloy and its Rietveld analysis (see Fig.S1 in Supplementary Information file) showed the formation of a $PuNi_3$ type intermetallic compound $LaNdMgNi_9$ (S.G. $R\bar{3}m$; a = 5.0066(2), c=24.239(1) Å) as a major phase (88 wt. %). This compound is isostructural to the intermetallic alloy La_2MgNi_9 [31]. In addition, two secondary phases are observed: $La_{0.5}Nd_{0.5}MgNi_4$ (*$MgCu_4Sn$* type cubic structure; S.G. $F\bar{4}3m$; 6.4(2) wt. %) and $La_{0.5}Nd_{0.5}Ni_5$ (*$CaCu_5$* type hexagonal structure; S.G. *P6/mmm*; 5.6(2) wt. %). The lattice parameters of the constituent phases are listed in Table 2. The lattice parameter of the impurity cubic phase $La_{0.5}Nd_{0.5}MgNi_4$ (a = 7.1180(3) Å) is closer to that of the Nd-based $NdMgNi_4$ (a = 7.09875 Å) than that of La-based $LaMgNi_4$ (a = 7.18 Å) [38]. We assume that the ratio between La and Nd is 50/50; however, some deviation from that is possible and is impossible to judge on because of a very small amount of this phase being present.

As for the second impurity phase $La_{0.5}Nd_{0.5}Ni_5$, its structure resembles that of $LaNi_5$ (a=5.0274(2), c=3.9877(1) Å) [19] and $NdNi_5$ (a=4.9606(7), c=3.9746(4)Å) alloys [35]. As expected, the crystallographic characteristics of $La_{0.5}Nd_{0.5}Ni_5$ (a=4.991(1) and c=3.980(1) Å), were found to be intermediate between those for $LaNi_5$ and $NdNi_5$. During the refinements, we have assumed that the 1a site of the parent crystal structure is equally shared by La and Nd, according to the composition $La_{0.5}Nd_{0.5}Ni_5$.

Table 2. Cell and volume parameters for the phase constituents present in the intermetallic $LaNdMgNi_9$

Alloy	Space group	a (Å)	c (Å)	V (Å^3)	c/a	Ref.
$LaNdMgNi_9$	$R\bar{3}m$	5.0066(2)	24.239(1)	526.18(4)	4.84	This work
La_2MgNi_9	$R\bar{3}m$	5.0314(2)	24.302(1)	532.78	4.83	[31]
$La_{1.5}Nd_{0.5}MgNi_9$	$R\bar{3}m$	5.0258(1)	24.305(1)	531.66	4.83	[28]
$La_{0.5}Nd_{0.5}MgNi_4$	$F\bar{4}3m$	7.1180(3)	-	360.64	-	This work
$NdMgNi_4$	$F\bar{4}3m$	7.09875	-	357.72	-	[38]
$LaMgNi_4$	$F\bar{4}3m$	7.18	-	370.14	-	[38]
$La_{0.5}Nd_{0.5}Ni_5$	$P6/mmm$	4.991(1)	3.980(1)	85.86	0.797	This work
$LaNi_5$	$P6/mmm$	5.0274(2)	3.9877(1)	87.29	0.793	[19]
$NdNi_5$	$P6/mmm$	4.9606(7)	3.9746(4)	84.70	0.801	[35]

3.2 Neutron powder diffraction study of the crystal structure of $LaNdMgNi_9D_{12.9}$

The *PCT* absorption and desorption isotherm curves at 300 K of $LaNdMgNi_9$ are given in Fig. 1. The maximum capacity is 12.99 H/f.u., which corresponds to the hydrogen content of 1.54 wt. % H. The absorption isotherm shows a broad plateau at lower pressures (around 0.04 MPa). Another, much narrower plateau is located at a higher pressure (0.2-0.3 MPa). The first plateau is associated with a transformation from an α-solid solution of hydrogen in the intermetallic alloy to a β-hydride phase, leading to the formation of $LaNdMgNi_9D_{12.9}$. The higher plateau is related to the formation of the hydride of the secondary intermetallic $La_{0.5}Nd_{0.5}Ni_4Mg$. $La_{0.5}Nd_{0.5}Ni_5$ remains non-hydrogenated below 2.5 MPa.

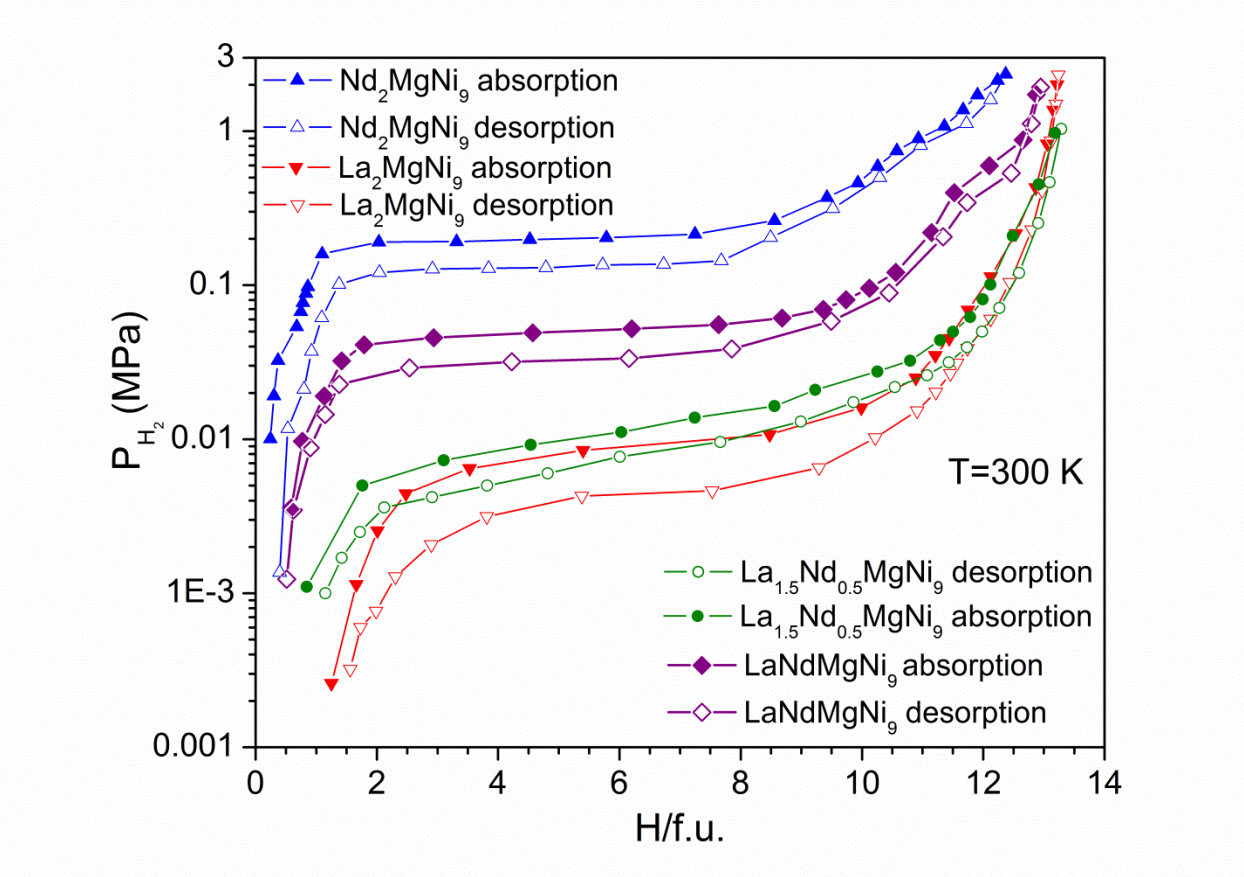

Figure 1. *PCT* isotherm curves at 300 K of the $LaNdMgNi_9$-H_2 system as compared to the reference data for La_2MgNi_9–H_2 [31], Nd_2MgNi_9–H_2 [34] systems.

The pressures of both absorption and desorption plateaus (see Figure 1) show a gradual increase with Nd content for the following compound series, La_2MgNi_9-$La_{1.5}Nd_{0.5}MgNi_9$-$LaNdMgNi_9$-Nd_2MgNi_9. The isotherms show that Nd-containing compounds have smaller absorption-desorption hysteresis as compared to La_2MgNi_9 leading to smaller energy losses. The reduction of the cell volume by 1.2 % taking place on La substitution by Nd in La_2MgNi_9 to form $LaNdMgNi_9$ (see Table 2) explains an increase in the plateau pressure in the *PCT* isotherms. The widening and flattening of the plateaus indicates a better homogeneity of the studied material showing that Nd can step up the voltage stability of the alloy electrode, which makes the Nd-containing $LaNdMgNi_9$ alloy more suitable as a metal hydride electrode.

Thermodynamic parameters of hydrogen desorption in the $LaNdMgNi_9$–H_2 system were calculated from the van't Hoff dependency (Fig. S2). Enthalpy and entropy changes for hydrogen desorption from the studied hydride are 30(1) kJ/mol H_2 and 94(3) J/K mol H_2, respectively. As expected, the thermodynamic stability of $LaNdMgNi_9$-based hydride appears to be intermediate between those for the $La_{1.5}Nd_{0.5}MgNi_9H_{13}$ and $Nd_2MgNi_9H_{12}$, which is reflected by the values of the equilibrium pressures of hydrogen desorption at room temperature (300 K),

0.01 MPa H_2 for $La_{1.5}Nd_{0.5}MgNi_9$, 0.04 MPa H_2 for $LaNdMgNi_9$, and 0.14 MPa H_2 for Nd_2MgNi_9.

The Rietveld refinement of the NPD pattern collected for the deuterated $LaNdMgNi_9$ alloy at constant D_2 pressure and room temperature conditions (1.6 MPa D_2; 300 K) is shown in Figure 2. Besides the diffraction peaks from the major phase constituent ($LaNdMgNi_9D_{12.9}$), two secondary phases are identified: $La_{0.5}Nd_{0.5}MgNi_4D_4$ and $La_{0.5}Nd_{0.5}Ni_5$ (the latter intermetallic did not absorb deuterium at the applied experimental conditions). The unit cell parameters of the constituent phases are listed in Table 3. The cell parameters of the deuterated impurity phase $La_{0.5}Nd_{0.5}MgNi_4D_4$ are in good agreement with the data given in reference [38].

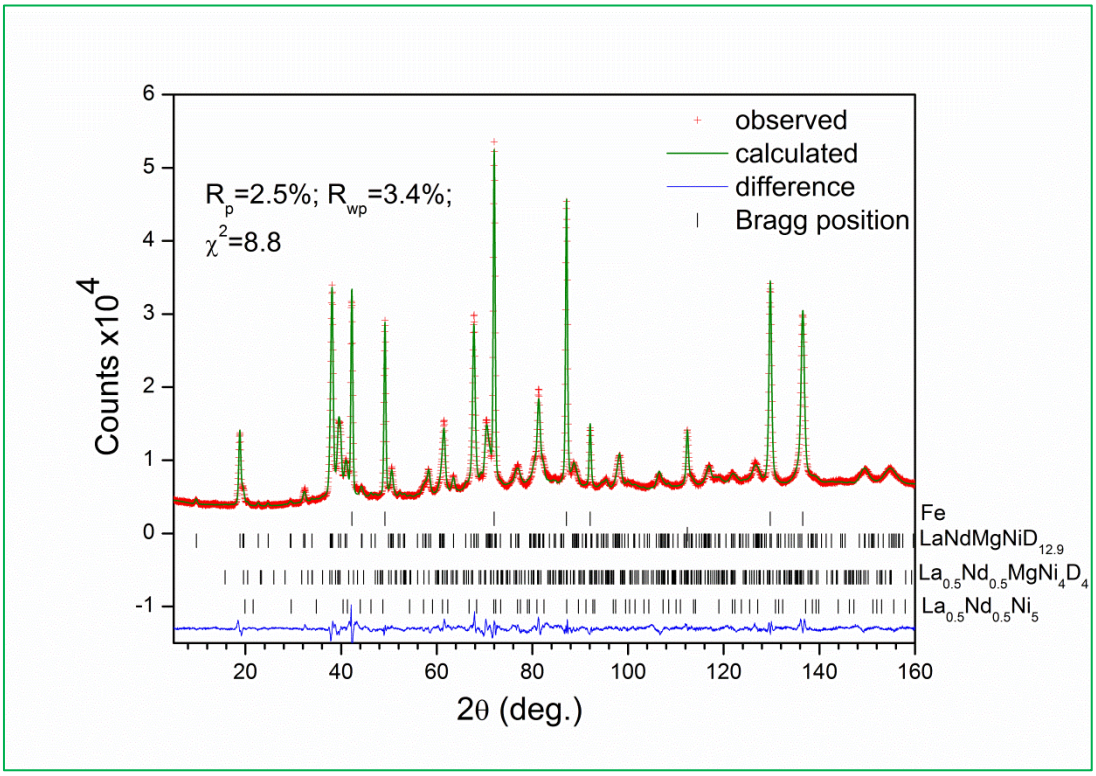

Figure 2. Rietveld refinements of the NPD pattern of $LaNdMgNi_9$ alloy saturated with deuterium. Wavelength used for NPD - λ=1.494 Å. The pattern show presence of three identified phase constituents, including $LaNdMgNi_9D_{12.9}$ - 91.3(2) wt.%, $La_{0.5}Nd_{0.5}MgNi_4D_4$ - 6.0(2) wt.%, $La_{0.5}Nd_{0.5}Ni_5$ - 2.7(2) wt.% and a stainless steel sample holder (Fe).

Table 3.

Space group, cell and volume parameters for the constituent phases present in the deuterated alloy $LaNdMgNi_9D_{12.9}$ as compared to the reference data.

Phase	Space group	*a*, Å	*b*, Å	*c*, Å	Volume, Å^3	Reference
$LaNdMgNi_9D_{12.9}$	$R\bar{3}m$	5.3672(1)	-	26.602(2)	663.65	This work
$La_2MgNi_9D_{13}$	$R\bar{3}m$	5.4151 (1)	-	26.584 (2)	675.10	[21]
$Nd_2MgNi_9D_{12}$	$R\bar{3}m$	5.3236(2)	-	26.506 (2)	650.55	[34]
$La_{0.5}Nd_{0.5}MgNi_4D_4$	$Pmn2_1$	5.131(3)	5.474(3)	7.413(5)	208.21	This work
$NdMgNi_4D_{3.6}$	$Pmn2_1$	5.0767 (2)	5.4743(2)	7.3792 (3)	205.08	[38]
$LaMgNi_4D_{3.7}$	$Pmn2_1$	5.12570(4)	5.52436(4)	7.45487(4)	211.09(2)	[39]

The crystallographic data for the $LaNdMgNi_9D_{12.9}$ deuteride are listed in Table 4. The crystal structure of $LaNdMgNi_9D_{12.9}$ (Fig.3) is similar to that reported for Nd-free $La_2MgNi_9D_{13}$ [21], with D atoms occupying both Laves A_2B_4 and Haucke AB_5 slabs. Three D-sites are located within the $(La/Nd)MgNi_4$ slab, two within the $(La/Nd)Ni_5$ slab and two D-sites are placed at the boundary between the $(La/Nd)MgNi_4$ and $(La/Nd)Ni_5$ slabs. The deuterium sub-lattice in the β-deuteride is composed of 7 filled sites, one less than Nd-free $La_2MgNi_9D_{13}$ [21]. All sites occupied by D atoms appear to be partially filled with occupancies ranging from 0.13 to 0.49. The calculated D content in $LaNdMgNi_9D_{12.9(3)}$ agrees well with that obtained from volumetric measurements (12.99(3) D/f.u.) performed during the synthesis of the deuteride.

In the Haucke AB_5 slab, D atoms fill two types of interstices with different metal surroundings: 2.80(5) D atoms are placed in the deformed D1 octahedra $[LaNdNi_4]$ and 0.60(2) D atoms are located in D2 tetrahedra $[Ni_4]$. Within the Laves A_2B_4 slab, D atoms exhibit three types of atomic coordination: D5 trigonal bipyramid $[(La,Nd/Mg)_3Ni_2]$; D6 tetrahedral $[(La/Nd/Mg)_2Ni_2]$ and D8 tetrahedral $[Ni_4]$. In addition, at the interface between the AB_5 and A_2B_4 layers tetrahedral $[(La/Nd/Mg)_2Ni_2]$ sites are occupied by D3 and D4 atoms. The D7 site with a tetrahedral atomic coordination $[(La/Mg)Ni_3]$, which is occupied in the structure of $La_2MgNi_9D_{13}$, remains vacant, in contrast with the structure of $La_2MgNi_9D_{13}$ [34] where an occupancy of 0.12(1) was reported.

The secondary phase $La_{0.5}Nd_{0.5}MgNi_4$ was assumed to contain around 4 D/f.u, resembling the $NdMgNi_4$-based hydride containing 3.6 at.H/f.u. [38]. The *a* and *c* lattice parameters of the mixed (La+Nd) phase are larger than that for $NdMgNi_4D_{3.6}$ [38]. As the contribution from impurity phases (especially from $La_{0.5}Nd_{0.5}Ni_5$) is very small, these phases were not refined except for the weight fractions.

Table 4.

Structural data of $LaNdMgNi_9D_{12.9}$ obtained from Rietveld refinements (agreement factors R_{wp}=3.4%, R_p=2.5%; χ^2=8.8) of the neutron diffraction pattern (300 K, 1.6 MPa D_2). S.G. $R\bar{3}m$ (No.166); a = 5.3672(1) Å, c = 26.602(2) Å, V = 663.65(5) Å^3.

Atom	Wyckoff positions	x/a	y/b	z/c	U_{iso}×100 (Å^2)	Occupancy
(La/Nd)1	3*a*	0	0	0	0.6(3)	0.5/0.5(–)
(La/Nd)2/Mg	6*c*	0	0	0.1408(3)	2.6(2)	(0.25/0.25)/0.5(–)
Ni1	3*b*	0	0	½	1.1(2)	1.0(–)
Ni2	6*c*	0	0	0.3285(2)	1.5(1)	1.0(–)
Ni3	18*h*	0.4982(5)	–*x*	0.0834(1)	1.02(4)	1.0(–)
D1	36*i*	0.538(3)	0.544(3)	0.0166(4)	2.32(9)	0.233(4)
D2	6*c*	0	0	0.3889(8)	2.32(9)	0.30(1)
D3	18*h*	0.182(5)	–*x*	0.0702(5)	2.32(9)	0.133(9)
D4	18*h*	0.848(1)	–*x*	0.0704(5)	2.32(9)	0.49(1)
D5	18*h*	0.496(1)	–*x*	0.1483(3)	2.32(9)	0.487(7)
D6	18*h*	0.829(2)	–*x*	0.0989(6)	2.32(9)	0.34(1)
D7	6c	0	0	0.235	-	vacant
D8	6*c*	0	0	0.4424(6)	2.32(9)	0.40(2)

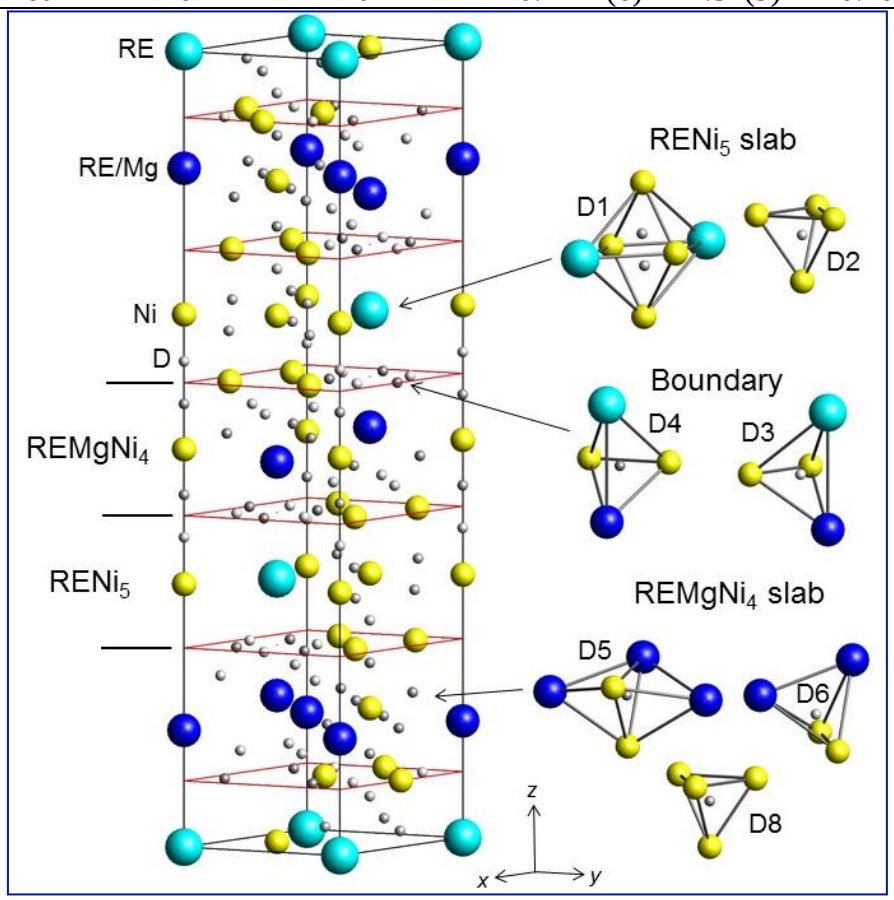

Figure 3. Crystal structure of $LaNdMgNi_9D_{12.9}$ showing the stacking of the (La,Nd)Ni_5 and (La,Nd, Mg)Ni_4 slabs. La and Nd are labelled as *RE* (rare earth metals). The vacant D7 site is not shown. From 7 sites filled by D, two are located inside the (La/Nd)Ni_5 layer (D1, D2), three

inside the (La/Nd)$MgNi_4$ layer (D5, D6, D8), and two at the boundary between the two slabs (D3, D4).

3.3 Electrochemical studies of $LaNdMgNi_9$ alloy

3.3.1 Discharge capacity characteristics of the alloys

The electrochemical properties of $LaNdMgNi_9$ as an anode electrode material, including its discharge capacity, activation performance, cycle stability, current density dependence and electrochemical impedance spectroscopy (EIS) data, were studied. After the activation, a discharge capacity of 364 mAh/g was reached at a current density of 1/3 *C* (see Fig.4 (a)).

The discharge curve shows a flat and long plateau of discharge between -0.85 V and -0.89 V. This is in a good agreement with the flat plateau observed in the *PCT* experiments (Figure 1). The electrochemical discharge capacity of $LaNdMgNi_9$ at 1/6 *C* rate (373 mAh/g) slightly decreases compared to that of the Nd-free compound La_2MgNi_9 (400 mAh/g) (see Fig.S3). On increasing the discharge rate up to 2.3 *C* rate, the discharge capacity goes down to 248 mAh/g, which can be still considered a good performance for such a high kinetic regime. Indeed, this is confirmed by high-rate dischargeability (HRD) studies on $LaNdMgNi_9$. In Figure 4(b), HRD results are compared to those of Nd-free La_2MgNi_9. The Nd-containing alloy electrode exhibits an obvious increase in HRD properties, particularly at high *C* rates. The origin of this improvement can be assigned to the increase in absolute value of the mid plateau potential caused by the lattice contraction that results from the partial Nd for La substitution. The higher hydrogen desorption pressure of the Nd-containing hydride facilitates the hydrogen exchange rate, enhancing the HRD [40].

The cyclic stability of the $LaNdMgNi_9$ electrode was studied at a kinetic rate of *C* with 100% depth of discharge (DOD). The discharge capacity decay was determined to be 27% after 300 cycles (see Fig.S4). The electrode performance of the $LaNdMgNi_9$ alloy showed a slightly better cyclic stability as compared to $La_{1.5}Nd_{0.5}MgNi_9$. The cyclic stability of the studied electrode material is restricted by its corrosion resistance. Corrosion leads to the formation of $Mg(OH)_2$ and $La(OH)_3$ hydroxides at the particle surfaces during the repeating charge-discharge cycles. Nd addition improves the resistance to oxidation but volumetric expansion of hydrogenation of the $LaNdMgNi_9$ appears to be lower as compared to La_2MgNi_9 (23.4 % vs. 26.71 %). Thus, lower pulverisation should be expected for the Nd containing intermetallic during hydrogen absorption. A decreased pulverization together with a better corrosion resistance will improve the cyclic stability, because of the decrease in the surface area and a reduction of the specific corrosion rate.

Improved cycling stability and HRD of $LaNdMgNi_9$ in comparison with our earlier study of $La_{1.5}Nd_{0.5}MgNi_9$ [28] show that a partial replacement of La by Nd in La_2MgNi_9 results in improved electrochemical performance, related to the Nd content.

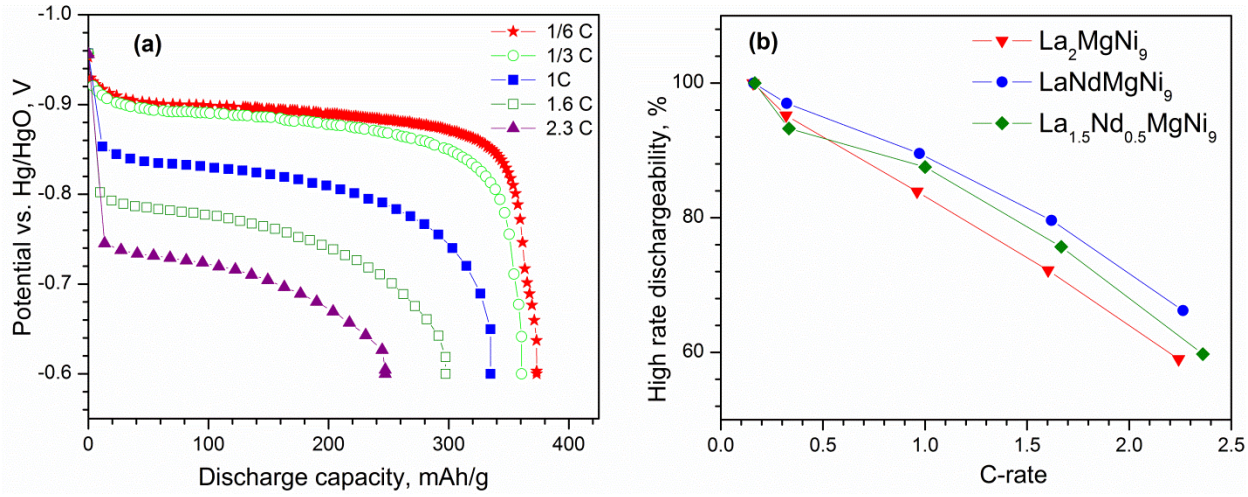

Figure 4. (a) Discharge capacities of the $LaNdMgNi_9$ electrode as a function of applied current densities; (b) HRD of $LaNdMgNi_9$ at different current densities in comparison with La_2MgNi_9 [19] and $La_{1.5}Nd_{0.5}MgNi_9$ [28].

3.3.2 Electrochemical Impedance Spectroscopy (EIS) studies

As a result of the degradation of the electrodes and electrolyte, the performance of the battery deteriorates while cycling. In order to quantify the electrochemical process behind the capacity deterioration of the anode electrode, we used Electrochemical Impedance Spectroscopy (EIS) as a tool to measure the changes in the battery characteristics.

EIS data appears to be highly dependent on the state of charge/discharge. Thus, we performed EIS measurements at the same state of discharge of 50 % DOD. The electrodes were cycled at *C* (300 mA/g). The EIS Nyquist plots for the $LaNdMgNi_9$ electrode subjected to a different number of galvanostatic cycles are shown in Fig.5. All EIS spectra display a semi-circle at high and middle frequencies and straight line dependence at low frequencies. Depending on the cycling history, there are clear differences in the spectra. As expected, a significant increase in the impedance resistance is observed with cycling in the high frequency region. This could be clearly seen in the magnitude Bode diagram shown in Figure S5.

The EIS data were analysed based on the fitting using an equivalent circuit shown in Fig.S7. The constant phase element (*Q*) was used to substitute the capacitance of electric double layer and the diffusion impedance for the decomposition of the electrolyte, and the results of the fitting of the impedance spectra are listed in Table 5 and Fig.S5-S8.

*R*1 is the electrolyte resistance between the working and the reference electrode. The constant phase element was used to substitute the capacitance of an electric double layer (*Q*1 and Q2). Two modelling parameters, resistance *R*2 and capacitance *Q*1 (*C*1) influence the semi-circle part of the spectra in the high frequency region. These semi-circle segments are related to the contact

resistance between the electrode and the current collector. $R3$ is the resistance of the charge transfer reaction (oxidation/reduction process) over the entire alloy surface while $W1$ is the Warburg term. $W1$ is related to the rate of hydrogen diffusion and is derived from the analysis of the straight line parts of the spectra in the low-frequency region.

The analysis of the EIS spectra allows drawing the following conclusions:

- Broadening of the semi-circles with cycling is observed and is related to the increase in the resistances $R2$ and $R3$ (see Table 5) of the electrodes, causing the fading of the electrochemical discharge capacity. $R2$ and $R3$ increased from 2.183 Ω and 0.276 Ω to 2.76 Ω and 0.349 Ω, respectively, when the cycle number raised from 20 to 358.

- The onsets of the transition from the hemicycles to straight lines regions in the EIS spectra (inset in Figure 5) shift to the lower frequencies with cycling. This can be translated to a reduction in hydrogen transport rates across the particles which are evident from the change in Warburg coefficient (σ) (see Table 5) and a corresponding lowering of the apparent hydrogen diffusion coefficient on cycling.

- The increase of the surface charge transfer resistance, $R3$, upon cycling is probably associated with the change of the surface composition due to the corrosion and a partial loss of the alloy particles from the electrode. The resistance $R3$ increases by 26.4% after 358 cycles.

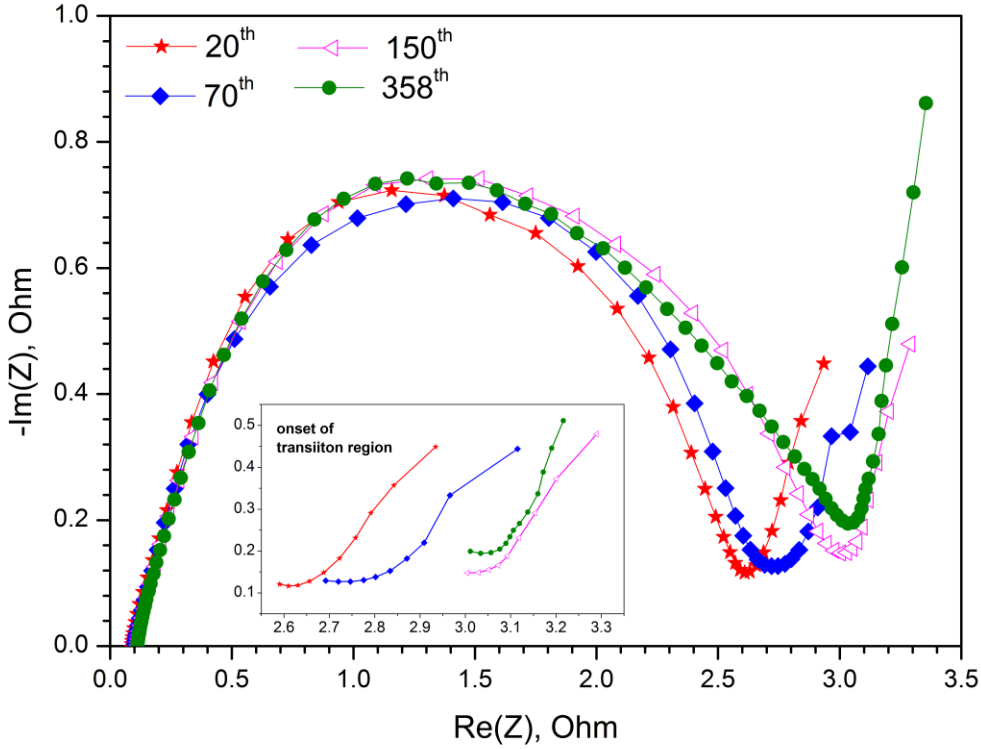

Figure 5. Nyquist plots for the $LaNdMgNi_9$ electrode after performing different number of cycles at 50% DOD. Current density used for cycling is 300mA/g. Inset shows the onset of transition regions.

Table 5. Refined parameters of the EIS for the spectra presented in Fig. 5.

Cycle number	Resistances, Ω			Warburg coefficient (σ), $\Omega s^{-1/2}$	Capacitance ($C2$), F
	$R1$	$R2$	$R3$		
20	0.087	2.183	0.276	0.032	0.0098
70	0.099	2.456	0.306	0.035	0.01386
150	0.111	2.623	0.332	0.023	0.01364
358	0.038	2.76	0.349	0.035	0.01574

3.4. *In operando* NPD study of the $LaNdMgNi_9$ alloy during electrochemical charge-discharge

Before the *in situ* experiments, the composite working electrode was first charged at a rate of $C/10$ (38 mA/g) for 12 h. Then, a galvanostatic discharge/charge cycle at $C/20$ rate (19 mA/g; see Fig.S9) was performed during *in-situ* neutron acquisition at PSI. Between discharge and charge sweeps, the electrodes were allowed to rest in open circuit potential (OCV) for 2 h.

The potential trace and charge capacity evolution on cycling is shown in Fig. 6. After 1 h of OCV with a rest potential of -0.14 V *vs* $E_{Cd/Cd(OH)2}$, the potential jumps to 0.05 V on applying a discharge current of 19 mA/g. Then, an inclined potential plateau is observed until the cut-off potential of 0.5 V. The electrochemical discharge capacity was 332 mAh/g. During the next rest period of 2 h the potential decreased to 0 V. Finally, on the charge sweep, the potential rapidly decreases below -0.2 V and remains constant, as result of the hydrogen evolution reaction.

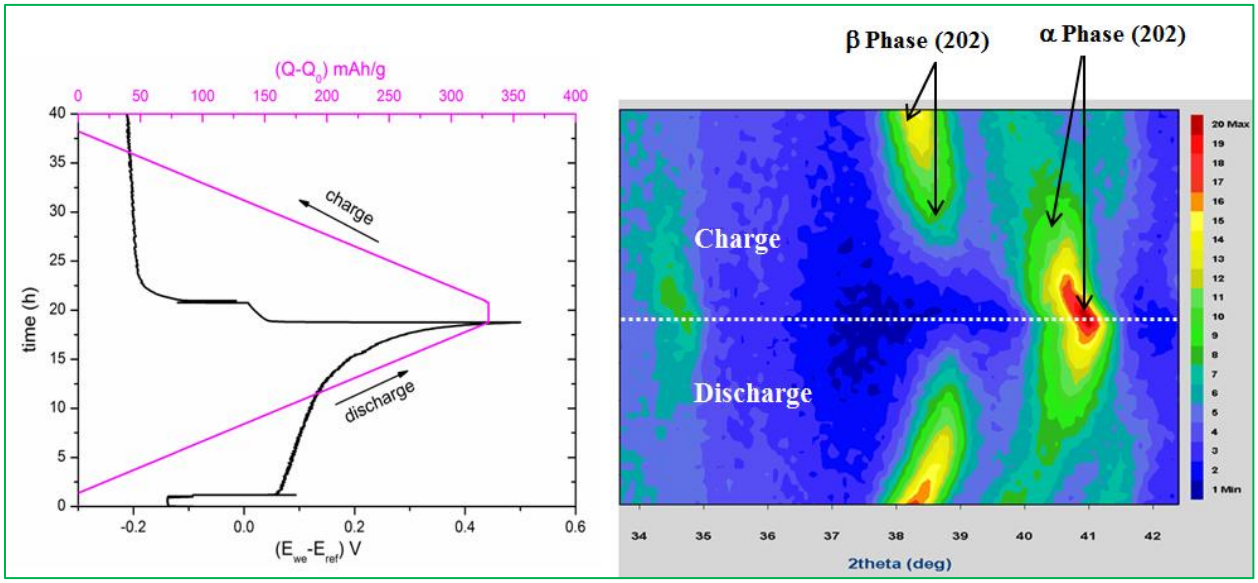

Figure 6. (Left) Discharge/charge potential profile and electrochemical capacity of the of the $LaNdMgNi_9$ electrode. (Right) 2D contour plot of NPD patterns within the angular domain 34°≤ 2θ ≤42° showing the evolution of (202) diffraction lines of α-metal and β-deuteride phases during galvanostatic cycling.

The evolution of NPD patterns within the angular range 34° ≤ 2θ ≤42° during galvanostatic cycling are displayed in Figure 6 right (2D contour plots). The diffraction patterns show presence of two phases: *alpha*-metal and *beta*-hydride. These phases practically coexist during the whole galvanostatic cycling.

The crystal structures of α and β phases were refined at half-discharge (electrochemical capacity 159 mAh/g, see Figure S9). The diffraction pattern (see Figure S10) was refined with two phases α-$LaNdMgNi_9D_{1.6}$ solid solution and β-$LaNdMgNi_9D_{8.2}$ deuteride both crystallizing in the $R\bar{3}m$ space group with unit cell parameters a = 5.032(3), c = 24.56(4) Å, V = 538.7(5) Å^3 and a = 5.266(2), c = 26.07(2) Å, V = 626.0(4) Å^3, respectively. The solid solution phase, α_{max}, corresponds to a saturated solid solution of deuterium in the metal and the hydride phase, β_{min}, to the most D-depleted deuteride. The results of the refinements of the NPD data for α_{max}-$LaNdMgNi_9D_{1.6}$ and β_{min}-$LaNdMgNi_9D_{8.2}$ are summarized in Tables S1 and S2, respectively.

As can be noted in Fig. 6 (right), the (202) Bragg peaks at 2θ = ~38.4° (β) and 2θ = ~40.16° (α) of both phases display large shifts during the electrochemical discharge, which indicates the occurrence of large solid solution domains. The evolution of the lattice constants of both phases as a function of discharge capacity was derived from the refinements of the diffraction patterns and is plotted in Figure 7. On discharge, the unit cell volume for the β phase exhibits a half parabolic dependence from the state of charge until a half discharge state is reached and then remains almost constant until the end of discharge. For the α-phase, the cell volume is constant until the half of the discharge and then it linearly decreases until reaching full discharge. During the discharge, the volume of the β phase decreases continuously; this indicates that the deuteride is progressively depleted of deuterium. By the end of discharge the volume becomes nearly constant, though slightly decreasing.

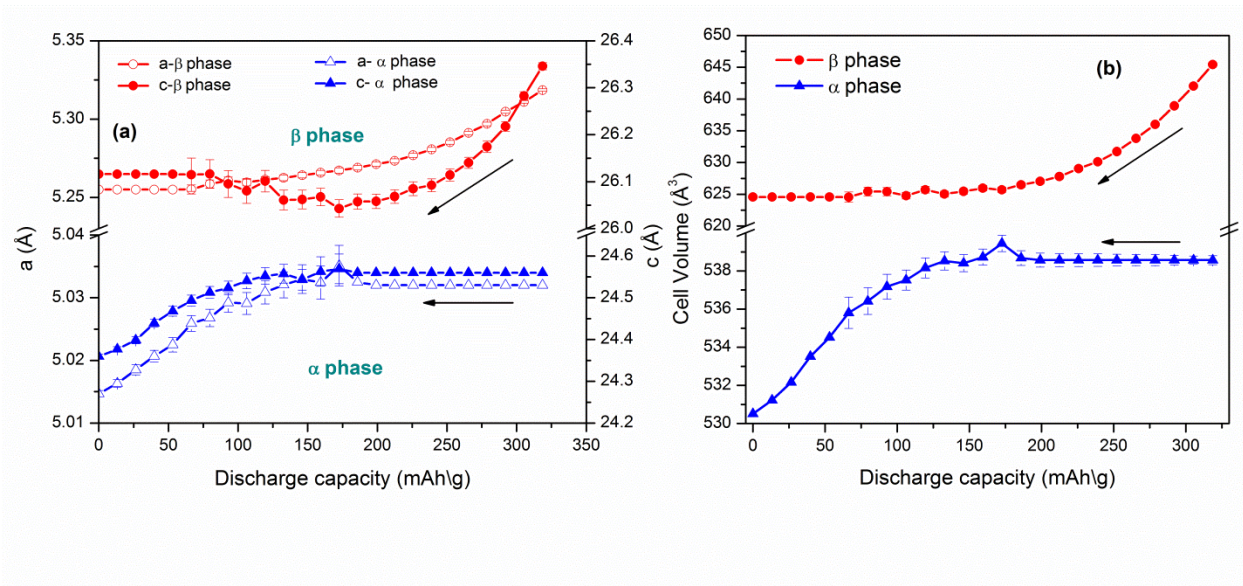

Figure 7. Evolution of the *a* and *c* lattice constants (a) and unit cell volumes *V* (b) for the α and β phases during the in-situ discharge cycle of the working electrode at *C*/20 (19 mA/g).

For the β-phase, the unit cell parameters at the state of charge were a = 5.3290(8) Å; c = 26.406(8) Å; V= 649.4 (2) Å^3 and the refined capacity is 9.8 D/f.u. These values are lower than for the fully saturated hydride synthesized using D_2 gas at a pressure of 1.6 MPa (Table 7), which is clearly associated with a depopulation of the specific sites occupied by D, D2 and D8, in the $LaNdMgNi_9D_{12.9}$ (see Table 6). A possible reason for that is that D2 and D8 sites have a tetrahedral Ni_4 surrounding. These sites are less attractive for hydrogen atoms as they are the smallest in size and are not coordinated by any hydride-forming rare earth nor magnesium atoms. The unit cell volume of the electrode material increases by 23.4% and 26.1% after the electrochemical charge and after the gas deuteration, respectively. In electrochemistry, we observe that the β-phase domain extends from $LaNdMgNi_9D_{9.8}$ to $LaNdMgNi_9D_{8.2}$. In this region, the volume contraction associated with deuterium depletion is quite high, ΔV/D = 4 Å^3,

much higher than normally observed during the formation of the metal hydrides, 2 to 3 Å^3/D. D atoms partially occupy five types of interstitial positions in both Laves and $CaCu_5$-type slabs. The D1 and D4 sites are located within the *RE*Ni_5 slabs, while three other sites (D5, D6 and D3) are within the *RE*$MgNi_4$ slabs. The crystal structure of the β deuteride is similar to the crystal structure of $Nd_2MgNi_9D_{12}$ reported by in our earlier study [34]. In both electrochemical and solid-gas cases, the D4 and D5 sites are the most occupied sites with occupancies of about 50%. The preferred filling of these sites by hydrogen is caused by the presence of more than 50 % of *RE* or Mg atoms in their surrounding (*RE*$MgNi_2$ for D4 and $(RE/Mg)_3Ni_2$ for D5). Figure S11 and table S3 show the D site occupancies for different sites, corresponding to the specific electrochemical capacities.

Table 6. Comparison between the D site occupancy of fully deuterated $LaNdMgNi_9$ intermetallic alloy by solid-gas reaction and electrochemical means.

D site	Surrounding	$LaNdMgNi_9D_{12.9}$ Occupancy (D_2 gas)	$LaNdMgNi_9D_{9.8}$ Occupancy (metal hydride anode)
D1	[*RE*Ni_3]	0.233(4)	0.087(2)
D2	[Ni_4]	0.30(1)	Vacant
D3	[(*RE*/Mg)*RE*Ni_2]	0.133(9)	0.286(3)
D4	[(*RE*/Mg)*RE*Ni_2]	0.49(1)	0.447(3)
D5	[$MgNi_2$]	0.487(7)	0.5
D6	[*RE*$MgNi_2$]/[$MgNi_2$]	0.34(1)	0.227(4)
D7	[(*RE*/Mg)Ni_3]	vacant	Vacant
D8	[Ni_4]	0.40(2)	Vacant

The refinements of the unit cell parameters and D site occupancies for the $\underline{\alpha}$ phase indicate, on discharge, the occurrence of the α-solid solution extending from 1.6 to 0.8 D/f.u. Such a solubility range is similar to our earlier observation for La_2MgNi_9 [31], where we concluded formation of α- $La_2MgNi_9H_1$ instead of a complete H/D depopulation to form initial intermetallic alloys. At the solubility limit ($LaNdMgNi_9D_{1.6}$) only 2 D sites (D1 and D4) are found to be occupied. The most occupied site is D4 ([$(RE/Mg)_2Ni_2$] surrounding), with occupancy 12%.

In summary, the following transformations were identified during the discharge of fully charged $LaNdMgNi_9D_{9.8}$ electrode:

β-$LaNdMgNi_9D_{9.8}$ + α_{max}-$LaNdMgNi_9D_{1.6}$ $\rightarrow$ β_{min}-$LaNdMgNi_9D_{8.2}$ + α_{max}-$LaNdMgNi_9D_{1.6}$ $\rightarrow$ β_{min}-$LaNdMgNi_9D_{8.2}$ + α-$LaNdMgNi_9D_{0.8}$

As shown in Fig. 8, the phase amount ratio between α- and β-phases shows a linear variation with the capacity, essentially confirming the two phase $\beta \rightarrow \alpha$ transformation. During the

electrochemical charge, the reverse phase transformation route was observed, *i.e.* the $\alpha \rightarrow \beta$ phase transformation.

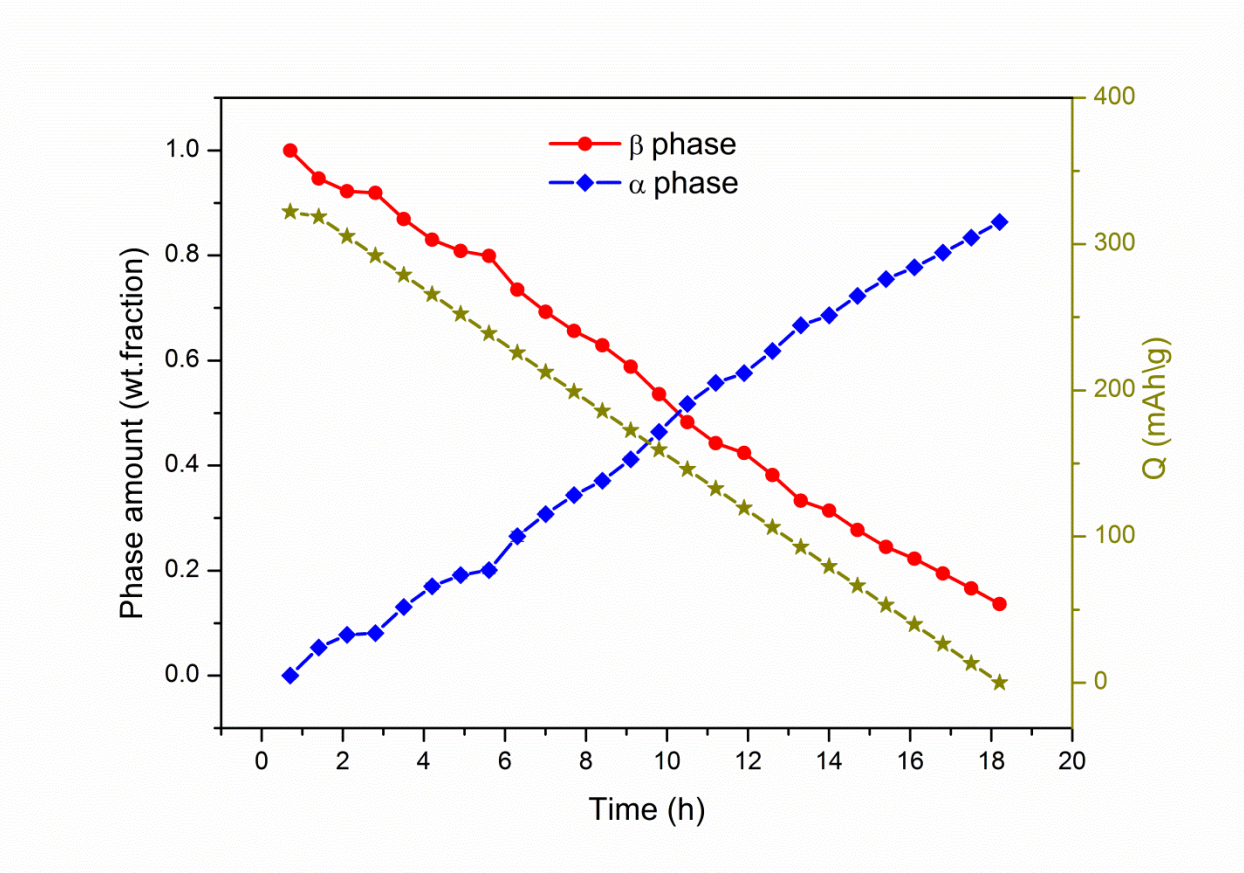

Figure 8. Phase behaviour of *alpha* and *beta* phases as a function of electrochemical discharge capacity during *in situ* discharge at *C*/10.

Table 7.Crystallographic data for the α- and β- phases observed during the electrochemical charge-discharge.

Compo-sition / Unit cell parameters	$LaNdMgNi_9$ (initial alloy)	$LaNdMgNi_9D_{0.8}$ (α_{min}-discharged saturated solid solution phase)	$LaNdMgNi_9D_{1.6}$ (α_{max}-discharged solid solution phase)	$LaNdMgNi_9D_{8.2}$ (β_{min}-deuteride received by electrochemical synthesis)	$LaNdMgNi_9D_{9.8}$ (β_{max}-deuteride saturated by D during electrochemical synthesis)	$LaNdMgNi_9D_{12.9}$ (β-deuteride; synthesized using D_2 gas at a pressure of 1.6 MPa)
a, Å	5.0066(2)	5.0147(5)	5.032(3)	5.267(2)	5.3290(8)	5.3672(1)
c, Å	24.239(2)	24.360(5)	24.56(4)	26.04(2)	26.406(8)	26.602(2)
V, $Å^3$	526.18(7)	530.5(1)	538.7(5)	625.7(4)	649.4(2)	663.65(5)
$\Delta a/a$, %	-	0.16	0.52	5.2	6.44	7.2
$\Delta c/c$, %	-	0.5	1.34	7.44	8.94	9.75
$\Delta V/V$, %	-	0.82	2.38	18.9	23.4	26.1

4. CONCLUSIONS

$LaNdMgNi_9$ crystallizes with a rhombohedral $PuNi_3$ type structure and has slightly lower unit cell parameters as compared to La_2MgNi_9. The partial replacement of La by Nd induces a volume contraction of 1.2 % for the metallic lattice. $LaNdMgNi_9$ displays a single pressure plateau in the *PCT* isotherm measured at 293 K, with a desorption pressure around 0.03 MPa H_2 and a maximum storage capacity close to 13 H/f.u.

The presence of Nd in the $La_{2-y}Nd_yMgNi_9$ alloys results in the appearance of more flat and longer plateaus, both in the case of hydrogen absorption-desorption and under electrochemical charge-discharge processes. Furthermore, increased Nd substitution for La in La_2MgNi_9 promotes the formation of a more homogeneous alloy and increases the high rate dischargeability (HRD) of the electrode. EIS studies of the electrode revealed that the reaction resistance is reduced after activation of the alloy and that hydrogen transport rate first is increased for the well activated electrode but then decreases on cycling because of degradation of the electrode.

Deuterium sorption properties of $LaNdMgNi_9$ were studied by solid-gas and electrochemical routes using *in situ* neutron powder diffraction. The electrochemically charged alloy showed a hydrogen storage capacity of 9.8 D/f.u, 23 % lower as compared to the deuteride obtained by solid-gas route at 1.6 MPa of deuterium pressure (12.9 D/f.u.). NPD studies of the saturated deuteride revealed a non-uniform distribution of D atoms within the *RE*$MgNi_4$ and *RE*Ni_5 layers and filling by D atoms of 7 types of interstitial sites.

During the electrochemical cycling, formation of an extended α–solid solution spanning from $LaNdMgNi_9D_{0.8}$ to $LaNdMgNi_9D_{1.6}$ was observed whereas the homogeneity range for the β-deuteride occurred between $LaNdMgNi_9D_{8.2}$ and $LaNdMgNi_9D_{9.8}$. The reversible cycling was accompanied by the discrete transformation between α- and β -phases. The same reaction pathway was observed during the charge and discharge yielding a completely reversible cycling of the metal hydride electrode. A fully discharged state (*i.e.*, 100% of the hydrogen-free intermetallic alloy) was not reached and the amount of electrochemically released hydrogen was significantly smaller than for the metal-gas interactions.

Comparison of the properties of the hydride materials containing a variable amount of Nd and increasing in a raw La_2MgNi_9-$La_{1.5}Nd_{0.5}MgNi_9$-$LaNdMgNi_9$-Nd_2MgNi_9, showed that presence of Nd is important to improve the anode electrodes of the RE_2MgNi_9 type and shows their clear advantages (broader and flatter plateaus, faster H exchange rates, better cycle stability and high rate discharge performance) over the Nd-free compositions. Further optimization of the Nd content in the $La_{2-y}Nd_yMgNi_9$ alloys will help in achieving the most efficient performance of the electrodes working in a high power regime.

ACKNOWLEDGEMENTS

This work was supported by Research Council of Norway and the European Spallation Source ((Project 234246 “HIGH POWER BATTERIES PROBED BY NEUTRON SCATTERING”).
The work is partly based on the experiments performed at the Swiss spallation neutron source SINQ, Paul Scherrer Institute, Villigen, Switzerland. We sincerely appreciate help from HRPT instrument responsible scientist Dr. D. Sheptyakov during the performed experiments.
We thank Dr. J.P. Mæhlen and Dr. P.J.S. Vie for their help in performing the EIS experiments and in the evaluation of the data.

Appendix A. Supplementary data

Supplementary data related to this article can be found at
http://dx.doi.org/10.1016/j.jpowsour.XXXX.XX.XXX.

REFERENCES

[1] H.Mua, F.Cheng, J.Chen, Wiley-VCH Verlag GmbH & Co. KGaA, Weinheim, Germany 1 & 2 (2011) 175-237.
[2] M. Armand, J.M. Tarascon, Nature 451 (2008) 652-657.
[3] J.J.G. Willems, Philips J.Res. 39 (1984) 1-94.
[4] M. Latroche , A. P-Guegan , Y. Chabre , J. Bouet , J. Pannetier , E. Ressouche, J.Alloys Compd. 231 (1995) 537-545.
[5] S.R.Ovshinsky, M.A.Fetcenko, J.Ross, Science 260 (1993) 176-181.
[6] Y.Liu, H. Pan, M.Gao, Q.Wang, J.Mater.Chem. 21 (2011) 4743-4755.
[7] R.V. Denys, A.B. Riabov, V.A. Yartys, M. Sato, R.G. Delaplane, J. Solid State Chem. 181 (2008) 812-821.
[8] T. Kohno, H. Yoshida, F. Kawashima, T. Inaba, I. Sakai, M. Yamamoto, M. Kanda, J. Alloys Compd. 311 (2000) L5-L7.
[9] I.E. Gabis, E.A. Evard, A.P. Voyt, V.G. Kuznetsov, B.P. Tarasov, J.C. Crivello, M. Latroche, R.V. Denys, W. Hu, V.A. Yartys, Electrochim. Acta 147 (2014) 73-81.
[10] B. Liao, Y.Q. Lei, L.X. Chen, G.L. Lu, H.G. Pan, Q.D. Wang, J. Power Sources 129 (2004) 358-367.
[11] Y. Liu, Y. Cao, L. Huang, M. Gao, H. Pan, J.Alloys Compd. 509 (2011) 675-686.
[12] T. Yang, Z. Yuan, W. Bu, Z. Jia, Y. Qi, Y. Zhang, Mater Design 93 (2016) 46-52.
[13] V. Yartys , D. Noreus, M. Latroche., Appl. Phys. A: Mater. Sci. Process. 122 (2016) 1-11.
[14] R.V. Denys, B. Riabov, V.A. Yartys, R.G. Delaplane, M. Sato, J. Alloys Compd. 446-447 (2007) 166-172.
[15] H. Miao, H. Pan, S. Zhang, N. Chen, R. Li, M. Gao, Int. J. Hydrogen Energy 32 (2007) 3387-3394.
[16] X. Zhang, D. Sun, W. Yin, Y. Chai, M. Zhao, J. Power Sources 154 (2006) 290-297.
[17] Y.-H. Zhang, X.-P. Dong, G.-Q. Wang, S.-H. Guo, J.-Y. Ren, X.-L. Wang, Int. J. Hydrogen Energy 32 (2007) 594-599.
[18] L. Xiao, Y. Wang, Y. Liu, D. Song, L. Jiao, H. Yuan, Int. J. Hydrogen Energy 33 (2008) 3925-3929.
[19] W.-K. Hu, R.V. Denys, C.C. Nwakwuo, T. Holm, J.P. Maehlen, J.K. Solberg, V.A. Yartys, Electrochim. Acta 96 (2013) 27-33.
[20] C. Wan, R.V. Denys, V.A. Yartys, J. Alloys Compd. 670 (2016) 210-216.
[21] R.V. Denys, V.A. Yartys, C.J. Webb, Inorg Chem 51 (2012) 4231-4238.
[22] Y. Li, D. Han, S. Han, X. Zhu, L. Hu, Z. Zhang, Y. Liu, Int. J. Hydrogen Energy 34 (2009) 1399-1404.
[23] H.Senoh, N.Takeichi, H.T.Tanaka, Qiang Xu, H.T. Takeshita, M.Toyouchi, T.Oishi, N. Kuriyama, Mater. Trans. 45 (2004) 292-295.
[24] J. Wang, S. Han, Y. Li, J. Liu, L. Che, L. Zhang, J. Zhang, J. Alloys Compd. 582 (2014) 552-557.
[25] L. Zhang, S.Cao, Y. Li, Y. Zhao, W.Du, Y.Ding, S.Hana, J. Electrochem. Soc. 162 (2015) A2218-A2226.
[26] Y. Li, S. Han, J. Li, X. Zhu, L. Hu, J. Alloys Compd. 458 (2008) 357-362.
[27] Q. Zhang, B. Zhao, M. Fang, C. Liu, Q. Hu, F. Fang, D. Sun, L. Ouyang, M. Zhu, Inorg Chem 51 (2012) 2976-2983.
[28] A.A. Volodin, C. Wan, R.V. Denys, G.A. Tsirlina, B.P. Tarasov, M. Fichtner, U. Ulmer, Y. Yu, C.C. Nwakwuo, V.A. Yartys, Int. J. Hydrogen Energy 41 (2016) 9954-9967.

[29] A.A. Volodin, R.V. Denys, G.A. Tsirlina, B.P. Tarasov, M. Fichtner, V.A. Yartys, J.Alloys Compd. 645 (2015) S288-S291.
[30] R.V. Denys, V.A. Yartys, J.Alloys Compd. 509 (2011) S540-S548.
[31] M. Latroche, F. Cuevas, W.-K. Hu, D. Sheptyakov, R.V. Denys, V.A. Yartys, J. Phys. Chem. C 118 (2014) 12162-12169.
[32] M.Latroche, Y.Chabre, B.Decamps, A. Percheron-Guegan, D. Noreus, J.Alloys Compd. 334 (2002) 267-276.
[33] R. Denys, V. Yartys, E. Gray, C. Webb, Energies 8 (2015) 3198-3211.
[34] V. Yartys, R. Denys, Chem. Met. Alloys 7 (2014) 1-8.
[35] V. Yartys, R. Denys, J. Alloys Compd. 645 (2015) S412-S418.
[36] B.H.Toby, J.Appl.Crystallogr. 34 (2001) 210-213.
[37] A.C.Larson, R.B.V. Dreele, Los Alamos National Laboratory Report LAUR (2004) 86-748.
[38] L.Guenee, V. Favre-Nicolin , K. Yvon, J.Alloys Compd. 348 (2003) 129-137.
[39] J.-N. Chotard, D. Sheptyakov, K. Yvon, Zeitschrift für Kristallographie 223 (2008).
[40] L. Zhang, W. Du, S. Han, Y. Li, S. Yang, Y. Zhao, C. Wu, H. Mu, Electrochim. Acta 173 (2015) 200-208.

Table 1

Table 1. Crystallographic, thermodynamic and electrochemical data for the $(La,Nd)_2MgNi_9$ systems

Alloy	Unit cell dimensions	H storage capacity, wt.% H	Plateau pressure, MPa (293 K)	ΔH (kJ/mol H_2) and ΔS (J/Kmol H_2)	Discharge capacity, mAh/g at $C/10$	Ref.
La_2MgNi_9	a = 5.0314 Å c = 24.302 Å V = 532.79 Å^3	1.5	0.005	ΔH = 35.9, ΔS = 96.7	375	[31]
$La_{1.5}Nd_{0.5}MgNi_9$	a = 5.0258 Å c = 24.305 Å V = 531.66 Å^3	1.4	0.01	-	410	[28]
Nd_2MgNi_9	a = 4.9783Å c = 24.1865Å V = 519.12 Å^3	1.46	0.14	ΔH = 28.6, ΔS = 99.5	-	[34]

Table 2

Table 2.

Cell and volume parameters for the phase constituents present in the intermetallic $LaNdMgNi_9$

Alloy	Space group	*a* (Å)	*c* (Å)	*V* (Å^3)	*c*/*a*	Ref.
$LaNdMgNi_9$	$R\bar{3}m$	5.0066(2)	24.239(1)	526.18(4)	4.84	This work
La_2MgNi_9	$R\bar{3}m$	5.0314(2)	24.302(1)	532.78	4.83	[31]
$La_{1.5}Nd_{0.5}MgNi_9$	$R\bar{3}m$	5.0258(1)	24.305(1)	531.66	4.83	[28]
$La_{0.5}Nd_{0.5}MgNi_4$	$F\bar{4}3m$	7.1180(3)	-	360.64	-	This work
$NdMgNi_4$	$F\bar{4}3m$	7.09875	-	357.72	-	[38]
$LaMgNi_4$	$F\bar{4}3m$	7.18	-	370.14	-	[38]
$La_{0.5}Nd_{0.5}Ni_5$	*P6/mmm*	4.991(1)	3.980(1)	85.86	0.797	This work
$LaNi_5$	*P6/mmm*	5.0274(2)	3.9877(1)	87.29	0.793	[19]
$NdNi_5$	*P6/mmm*	4.9606(7)	3.9746(4)	84.70	0.801	[35]

Table 3

Table 3.

Space group, cell and volume parameters for the constituent phases present in the deuterated alloy $LaNdMgNi_9D_{12.9}$ as compared to the reference data.

Phase	Space group	*a*, Å	*b*, Å	*c*, Å	Volume, Å^3	Reference
$LaNdMgNi_9D_{12.9}$	$R\bar{3}m$	5.3672(1)	-	26.602(2)	663.65	This work
$La_2MgNi_9D_{13}$	$R\bar{3}m$	5.4151 (1)	-	26.584 (2)	675.10	[21]
$Nd_2MgNi_9D_{12}$	$R\bar{3}m$	5.3236(2)	-	26.506 (2)	650.55	[34]
$La_{0.5}Nd_{0.5}MgNi_4D_4$	$Pmn2_1$	5.131(3)	5.474(3)	7.413(5)	208.21	This work
$NdMgNi_4D_{3.6}$	$Pmn2_1$	5.0767 (2)	5.4743(2)	7.3792 (3)	205.08	[38]
$LaMgNi_4D_{3.7}$	$Pmn2_1$	5.12570(4)	5.52436(4)	7.45487(4)	211.09(2)	[39]

Table 4

Table 4.

Structural data of $LaNdMgNi_9D_{12.9}$ obtained from Rietveld refinements (agreement factors R_{wp}=3.4%, R_p=2.5%; χ^2=8.8) of the neutron diffraction pattern (300 K, 1.6 MPa D_2). S.G. $R\bar{3}m$ (No.166); a = 5.3672(1) Å, c = 26.602(2) Å, V = 663.65(5) Å^3.

Atom	Wyckoff positions	x/a	y/b	z/c	U_{iso}×100 (Å^2)	Occupancy
(La/Nd)1	3*a*	0	0	0	0.6(3)	0.5/0.5(–)
(La/Nd)2/Mg	6*c*	0	0	0.1408(3)	2.6(2)	(0.25/0.25)/0.5(–)
Ni1	3*b*	0	0	½	1.1(2)	1.0(–)
Ni2	6*c*	0	0	0.3285(2)	1.5(1)	1.0(–)
Ni3	18*h*	0.4982(5)	–*x*	0.0834(1)	1.02(4)	1.0(–)
D1	36*i*	0.538(3)	0.544(3)	0.0166(4)	2.32(9)	0.233(4)
D2	6*c*	0	0	0.3889(8)	2.32(9)	0.30(1)
D3	18*h*	0.182(5)	–*x*	0.0702(5)	2.32(9)	0.133(9)
D4	18*h*	0.848(1)	–*x*	0.0704(5)	2.32(9)	0.49(1)
D5	18*h*	0.496(1)	–*x*	0.1483(3)	2.32(9)	0.487(7)
D6	18*h*	0.829(2)	–*x*	0.0989(6)	2.32(9)	0.34(1)
D7	6c	0	0	0.235	-	vacant
D8	6*c*	0	0	0.4424(6)	2.32(9)	0.40(2)

Table 5

Table 5.

Refined parameters of the EIS for the spectra presented in Fig. 5.

Cycle number	Resistances, Ω			Warburg coefficient (σ), $\Omega s^{-1/2}$	Capacitance ($C2$), F
	$R1$	$R2$	$R3$		
20	0.087	2.183	0.276	0.032	0.0098
70	0.099	2.456	0.306	0.035	0.01386
150	0.111	2.623	0.332	0.023	0.01364
358	0.038	2.76	0.349	0.035	0.01574

Table 6

Table 6.

Comparison between the D site occupancy of fully deuterated $LaNdMgNi_9$ intermetallic alloy by solid-gas reaction and electrochemical means.

D site	Surrounding	$LaNdMgNi_9D_{12.9}$ Occupancy (D_2 gas)	$LaNdMgNi_9D_{9.8}$ Occupancy (metal hydride anode)
D1	[*RE*Ni_3]	0.233(4)	0.087(2)
D2	[Ni_4]	0.30(1)	Vacant
D3	[(*RE*/Mg)*RE*Ni_2]	0.133(9)	0.286(3)
D4	[(*RE*/Mg)*RE*Ni_2]	0.49(1)	0.447(3)
D5	[$MgNi_2$]	0.487(7)	0.5
D6	[*RE*$MgNi_2$]/[$MgNi_2$]	0.34(1)	0.227(4)
D7	[(*RE*/Mg)Ni_3]	vacant	Vacant
D8	[Ni_4]	0.40(2)	Vacant

Table 7

Table 7.

Crystallographic data for the α- and β- phases observed during the electrochemical charge-discharge.

Composition / Unit cell parameters	$LaNdMgNi_9$ (initial alloy)	$LaNdMgNi_9D_{0.8}$ (α_{min}-discharged saturated solid solution phase)	$LaNdMgNi_9D_{1.6}$ (α_{max}-discharged solid solution phase)	$LaNdMgNi_9D_{8.2}$ (β_{min}-deuteride received by electrochemical synthesis)	$LaNdMgNi_9D_{9.8}$ (β_{max}-deuteride saturated by D during electrochemical synthesis)	$LaNdMgNi_9D_{12.9}$ (β-deuteride; synthesized using D_2 gas at a pressure of 1.6 MPa)
a, Å	5.0066(2)	5.0147(5)	5.032(3)	5.267(2)	5.3290(8)	5.3672(1)
c, Å	24.239(2)	24.360(5)	24.56(4)	26.04(2)	26.406(8)	26.602(2)
V, $Å^3$	526.18(7)	530.5(1)	538.7(5)	625.7(4)	649.4(2)	663.65(5)
$\Delta a/a$, %	-	0.16	0.52	5.2	6.44	7.2
$\Delta c/c$, %	-	0.5	1.34	7.44	8.94	9.75
$\Delta V/V$, %	-	0.82	2.38	18.9	23.4	26.1

Figure 1
Click here to download high resolution image

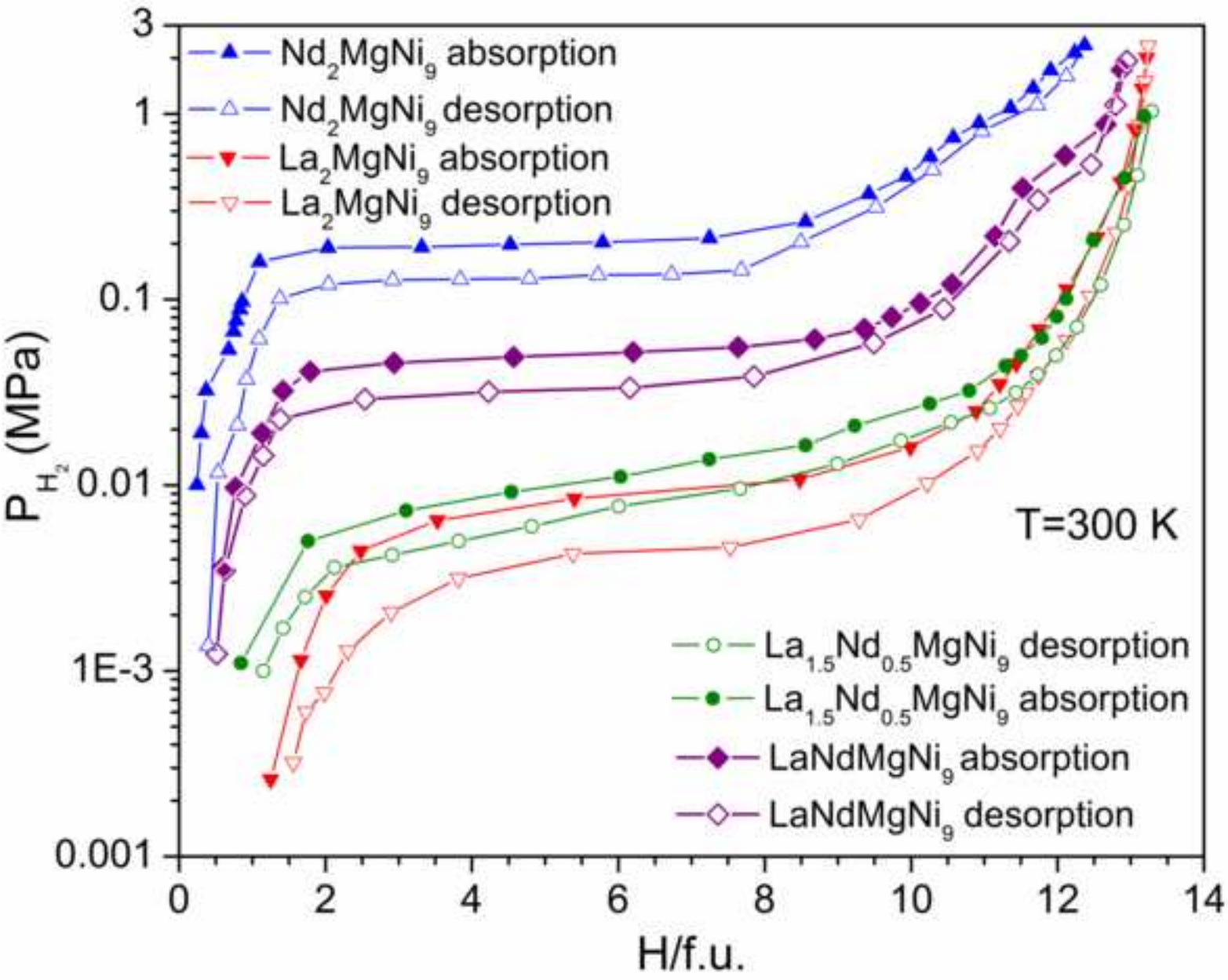

Figure 2
Click here to download high resolution image

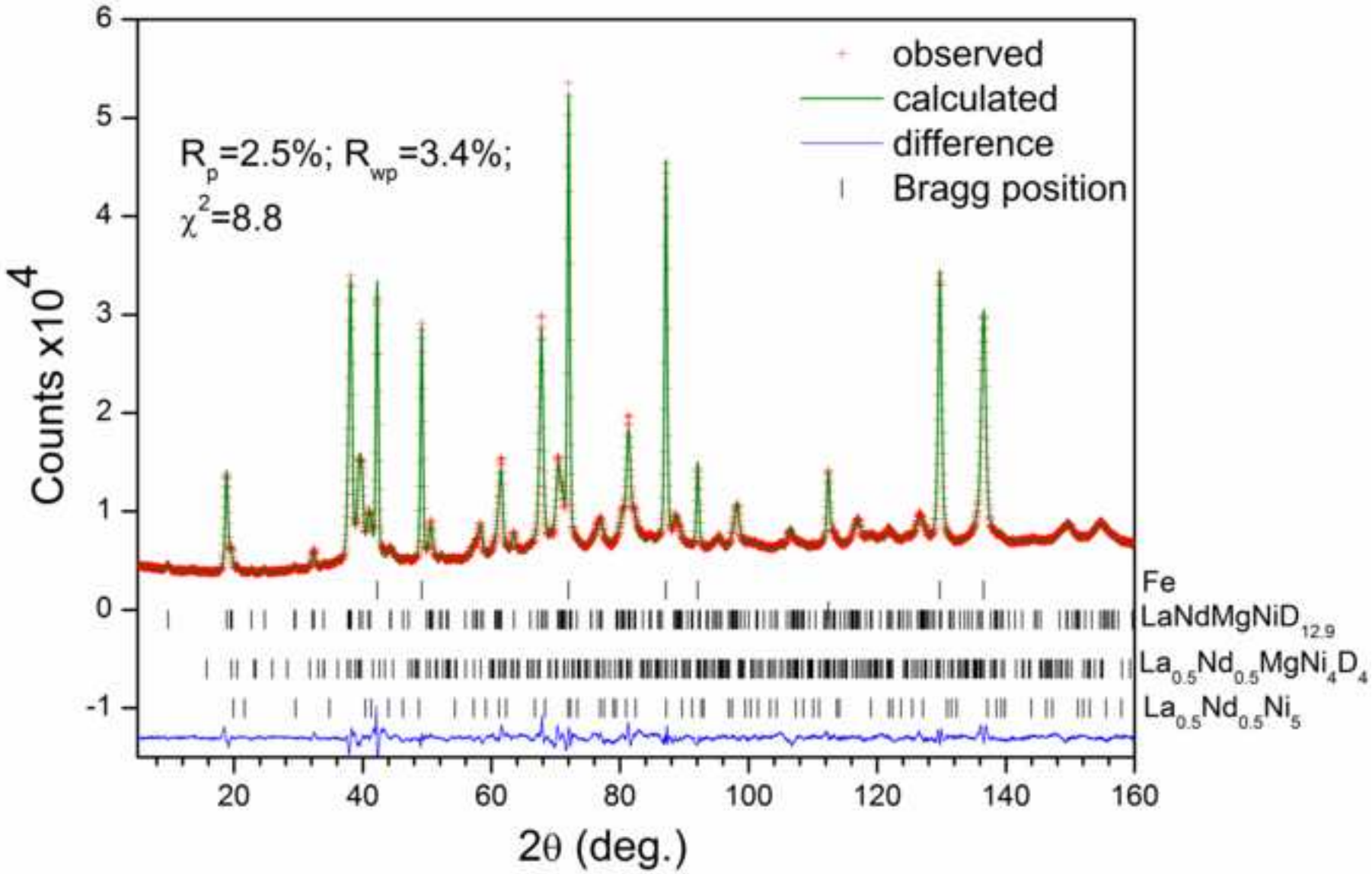

Figure 3
Click here to download high resolution image

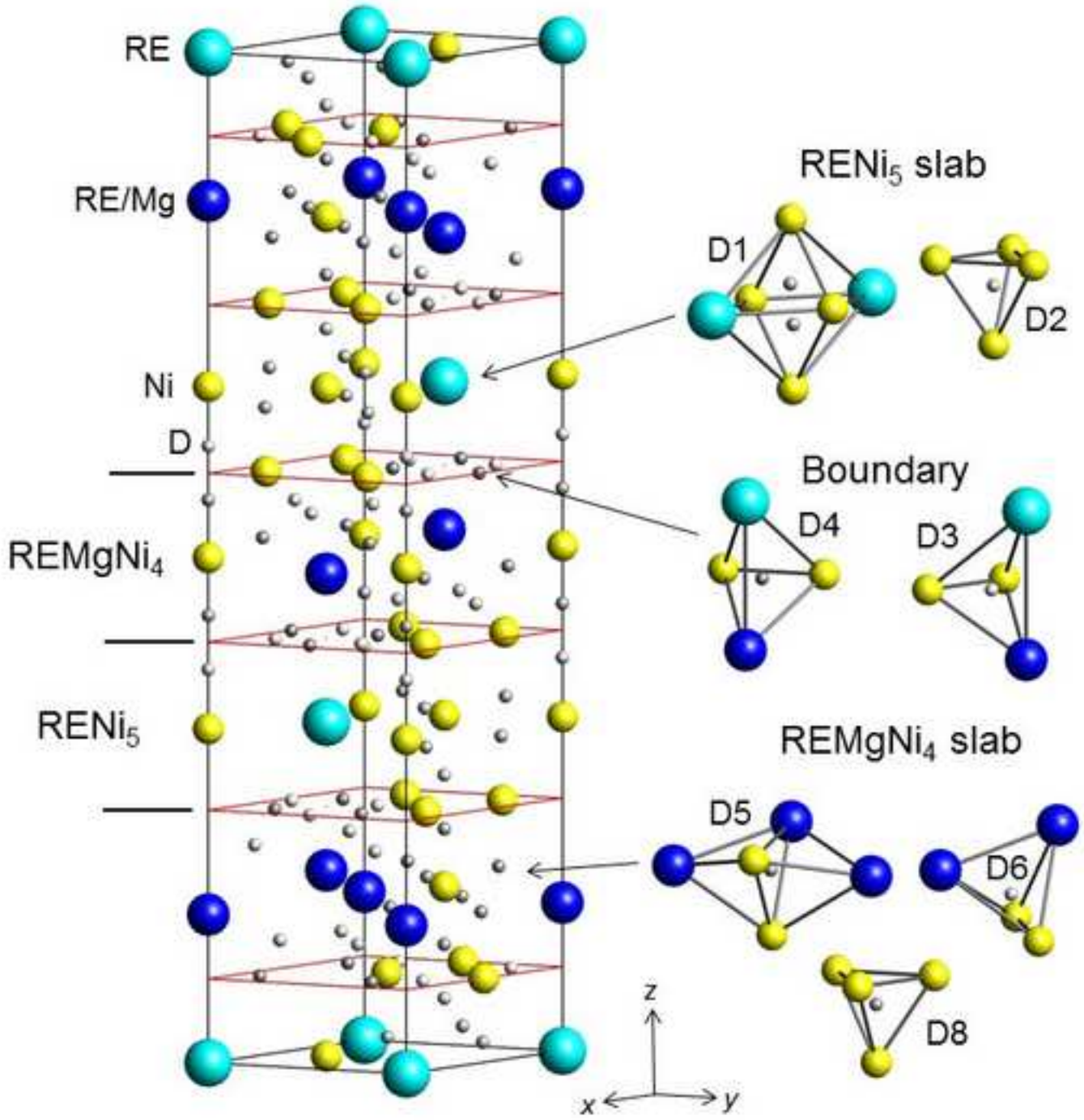

Figure 4
Click here to download high resolution image

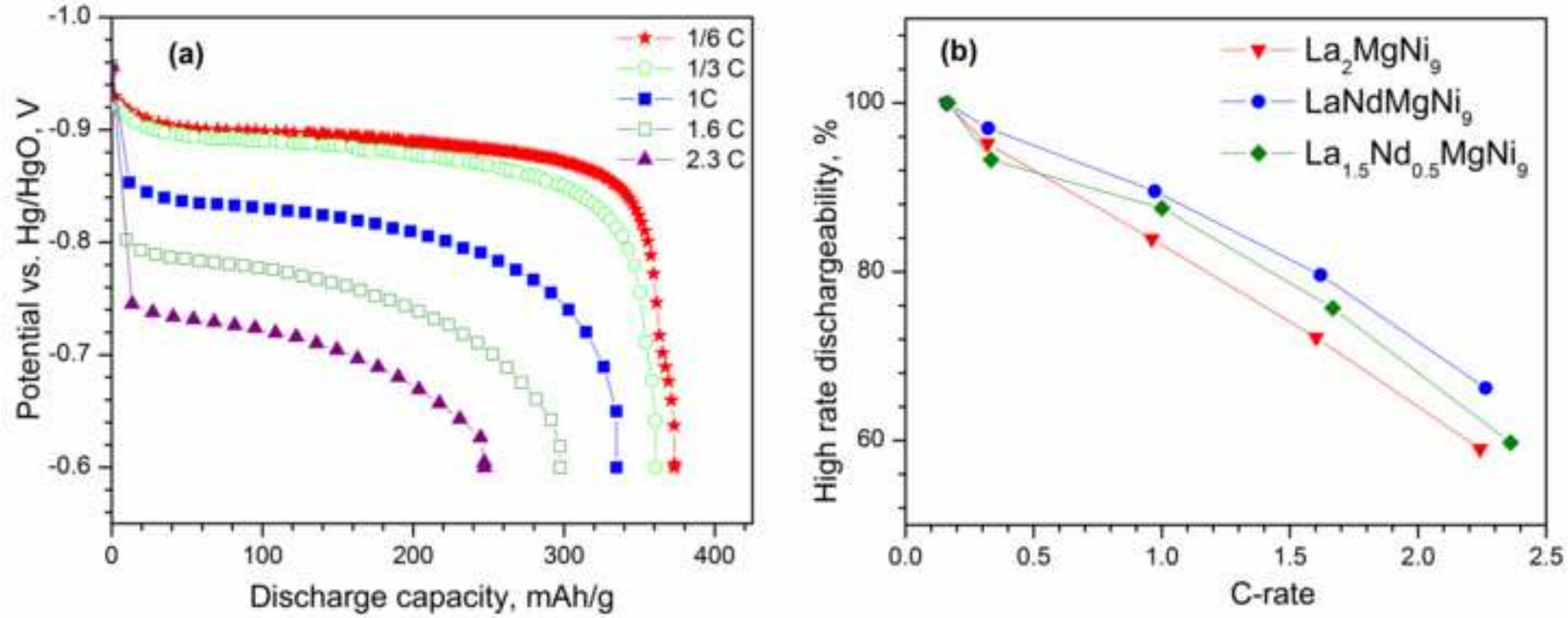

Figure 5
Click here to download high resolution image

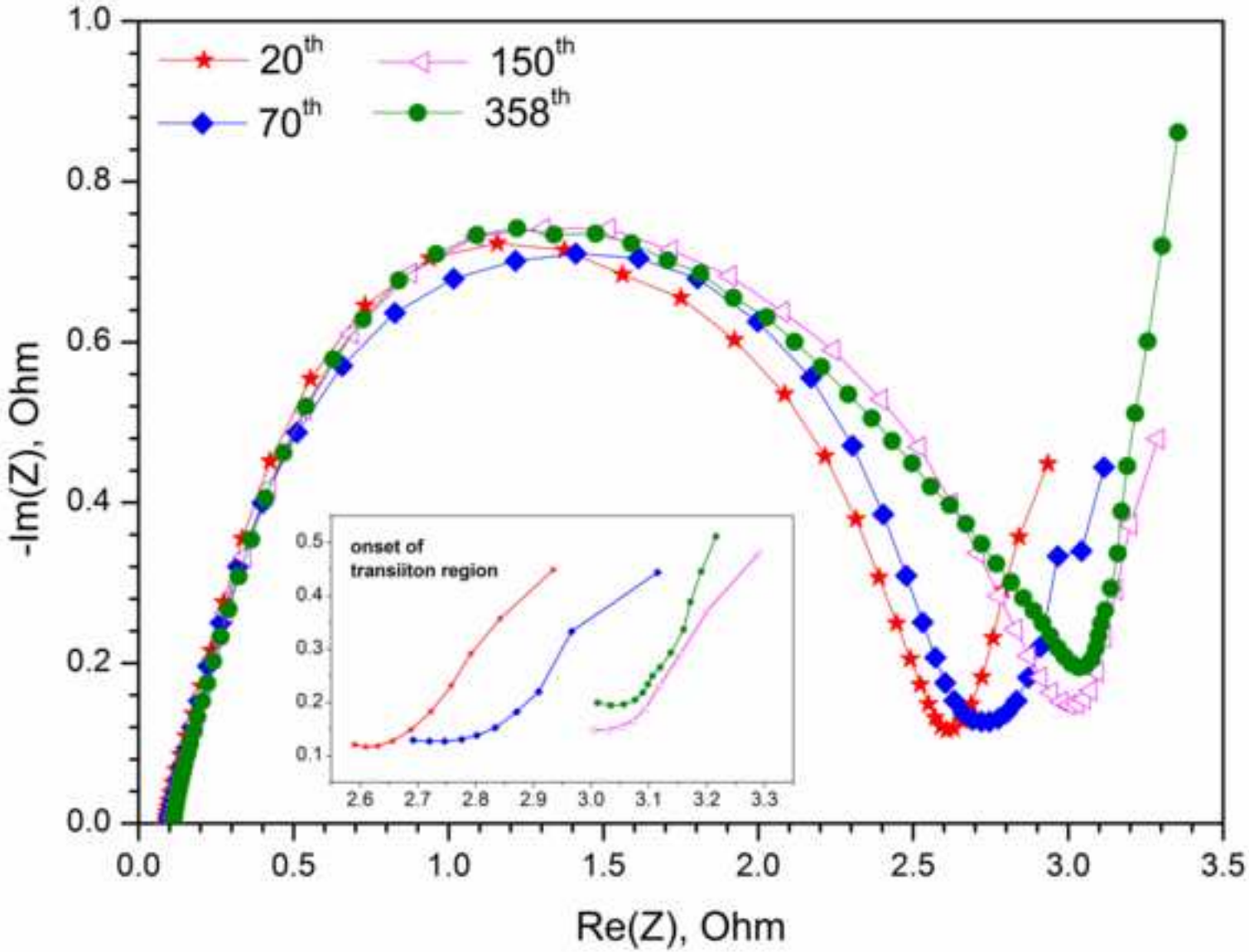

Figure 6

Click here to download high resolution image

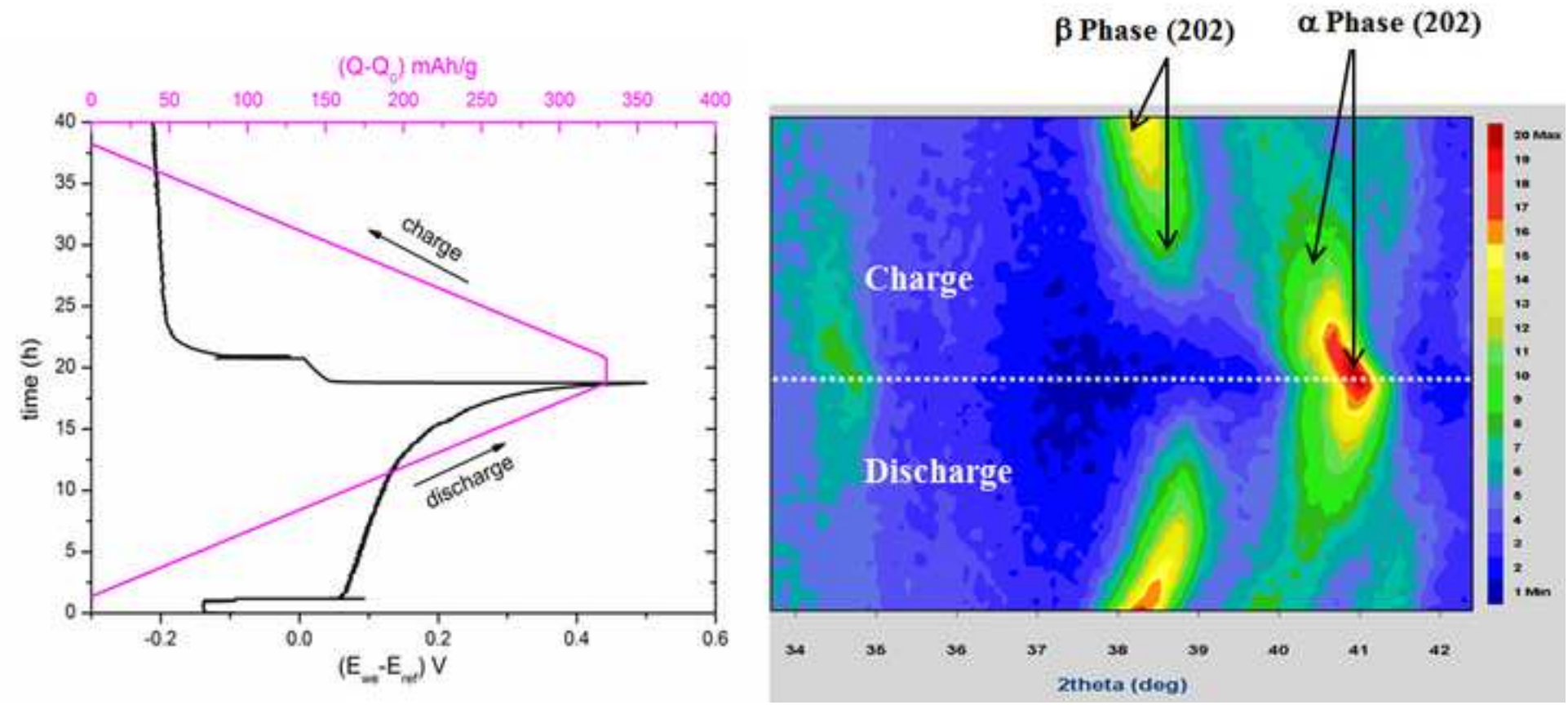

Figure 7
Click here to download high resolution image

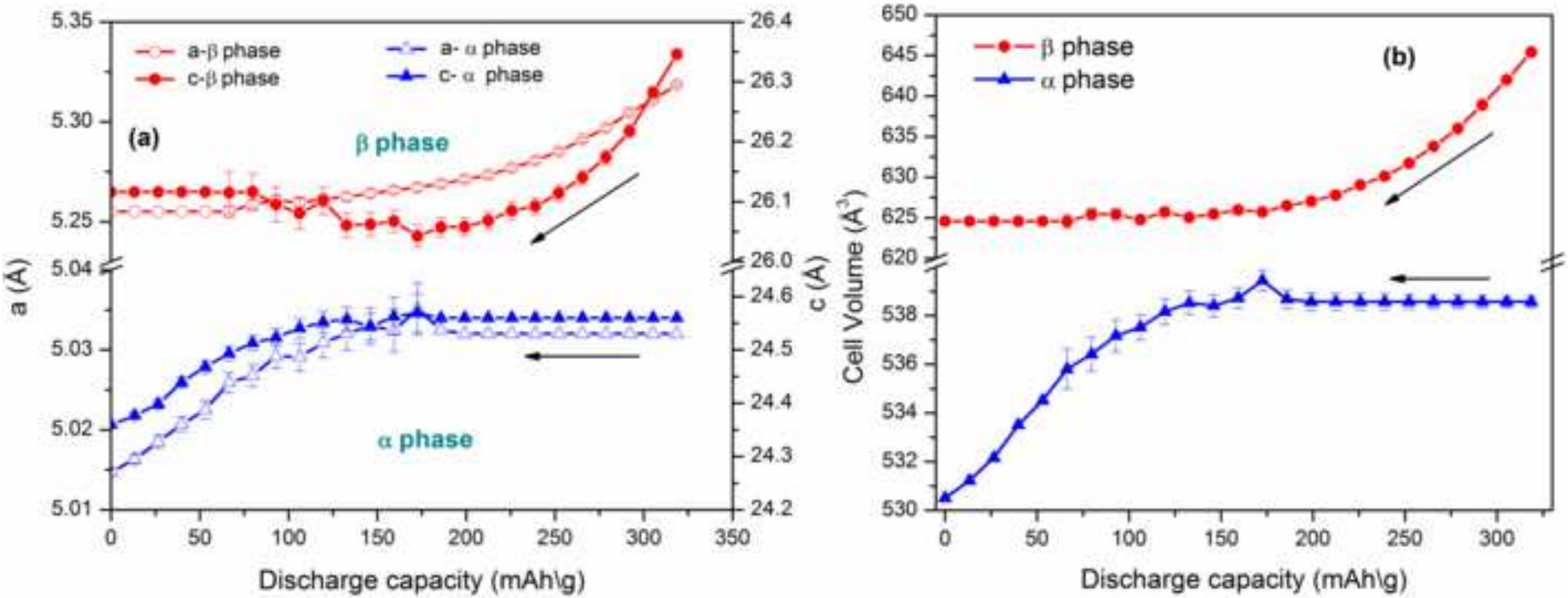

Figure 8
Click here to download high resolution image

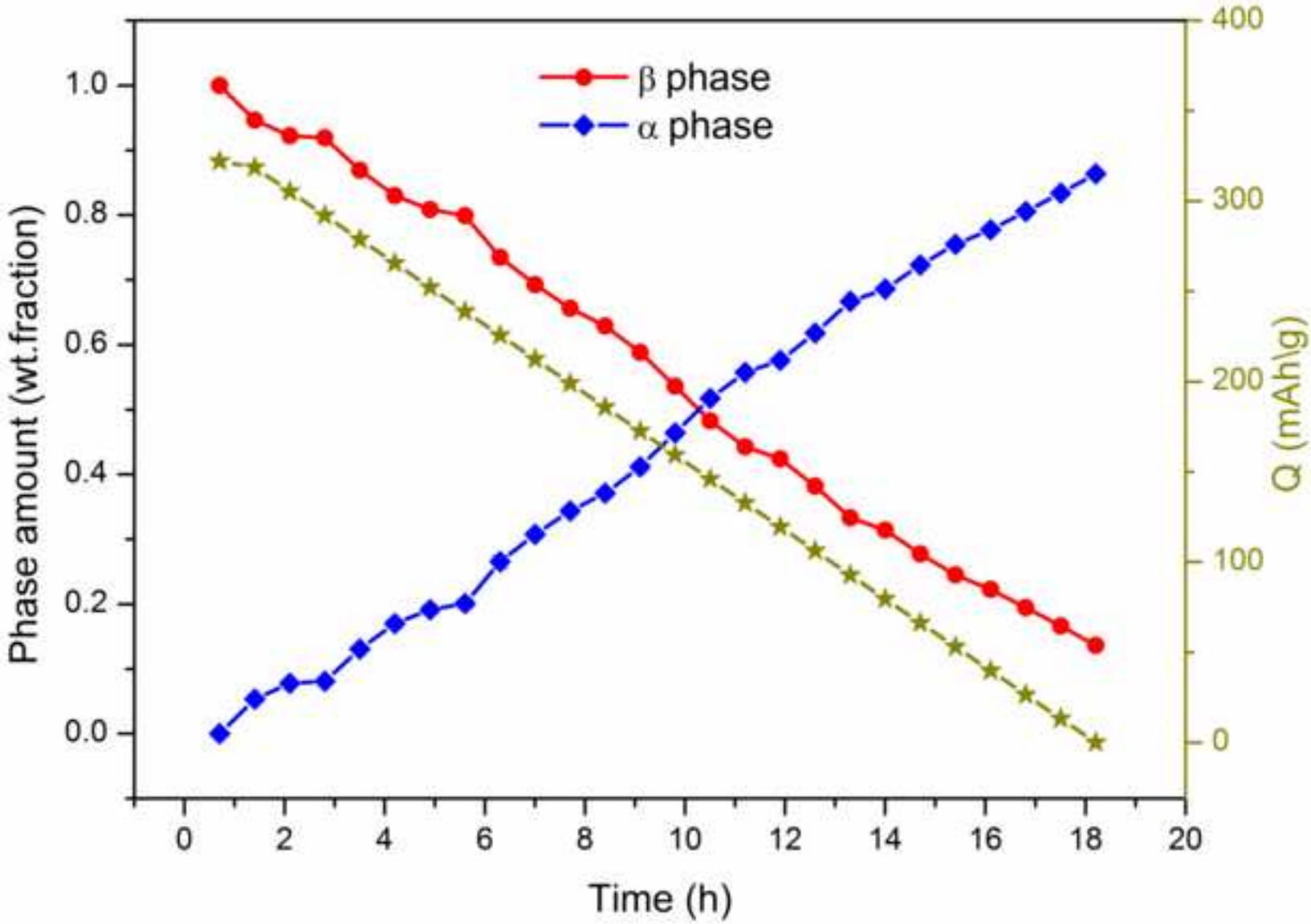

Figure captions in the manuscript

In operando neutron diffraction study of $LaNdMgNi_9$ as a metal hydride battery anode

by

N. S. Nazer, R.V. Denys, V.A. Yartys, Wei-Kang Hu,
M.Latroche, F.Cuevas, B.C. Hauback, P.F.Henry and L. Arnberg

Figure 1. *PCT* isotherm curves at 300 K of the $LaNdMgNi_9$-H_2 system as compared to the reference data for La_2MgNi_9–H_2 [31], Nd_2MgNi_9–H_2 [34] systems.

Figure 2. Rietveld refinements of the NPD pattern of $LaNdMgNi_9$ alloy saturated with deuterium. Wavelength used for NPD - λ=1.494 Å. The pattern show presence of three identified phase constituents, including $LaNdMgNi_9D_{12.9}$ - 91.3(2) wt.%, $La_{0.5}Nd_{0.5}MgNi_4D_4$ - 6.0(2) wt.%, $La_{0.5}Nd_{0.5}Ni_5$ - 2.7(2) wt.% and a stainless steel sample holder (Fe).

Figure 3. Crystal structure of $LaNdMgNi_9D_{12.9}$ showing the stacking of the $(La,Nd)Ni_5$ and $(La,Nd, Mg)Ni_4$ slabs. La and Nd are labelled as *RE* (rare earth metals). The vacant D7 site is not shown. From 7 sites filled by D, two are located inside the $(La/Nd)Ni_5$ layer (D1, D2), three inside the $(La/Nd)MgNi_4$ layer (D5, D6, D8), and two at the boundary between the two slabs (D3, D4).

Figure 4. (a) Discharge capacities of the $LaNdMgNi_9$ electrode as a function of applied current densities; (b) HRD of $LaNdMgNi_9$ at different current densities in comparison with La_2MgNi_9 [19] and $La_{1.5}Nd_{0.5}MgNi_9$ [28].

Figure 5. Nyquist plots for the $LaNdMgNi_9$ electrode after performing different number of cycles at 50% DOD. Current density used for cycling is 300mA/g. Inset shows the onset of transition regions.

Figure 6. (Left) Discharge/charge potential profile and electrochemical capacity of the of the $LaNdMgNi_9$ electrode. (Right) 2D contour plot of NPD patterns within the angular domain $34° \leq 2\theta \leq 42°$ showing the evolution of (202) diffraction lines of α-metal and β-deuteride phases during galvanostatic cycling.

Figure 7. Evolution of the *a* and *c* lattice constants (a) and unit cell volumes *V* (b) for the α and β phases during the in-situ discharge cycle of the working electrode at *C*/20 (19 mA/g).

Figure 8. Phase behaviour of *alpha* and *beta* phases as a function of electrochemical discharge capacity during *in situ* discharge at *C*/10.

Supplementary Materials

Click here to download Supplementary Materials: Supplemenatry file _FINAL_SUBMISSION.docx

SUPPLEMENTARY INFORMATION TO THE MANUSCRIPT

In operando neutron diffraction studies of $LaNdMgNi_9$ as anode for metal hydride battery

N. S. Nazer[1, 2], R.V. Denys[1], V.A. Yartys[1, 2 *], Wei-Kang Hu[1], M.Latroche[3], F.Cuevas[3], B.C. Hauback[1], P.F.Henry[4] and L. Arnberg[2]

(1) Institute for Energy Technology, Kjeller, Norway; (2) NTNU, Trondheim, Norway; (3) Université Paris East, ICMPE (UMR7182), CNRS, UPEC, F-94320 Thiais, France; (4) European Spallation Source ERIC, Sweden

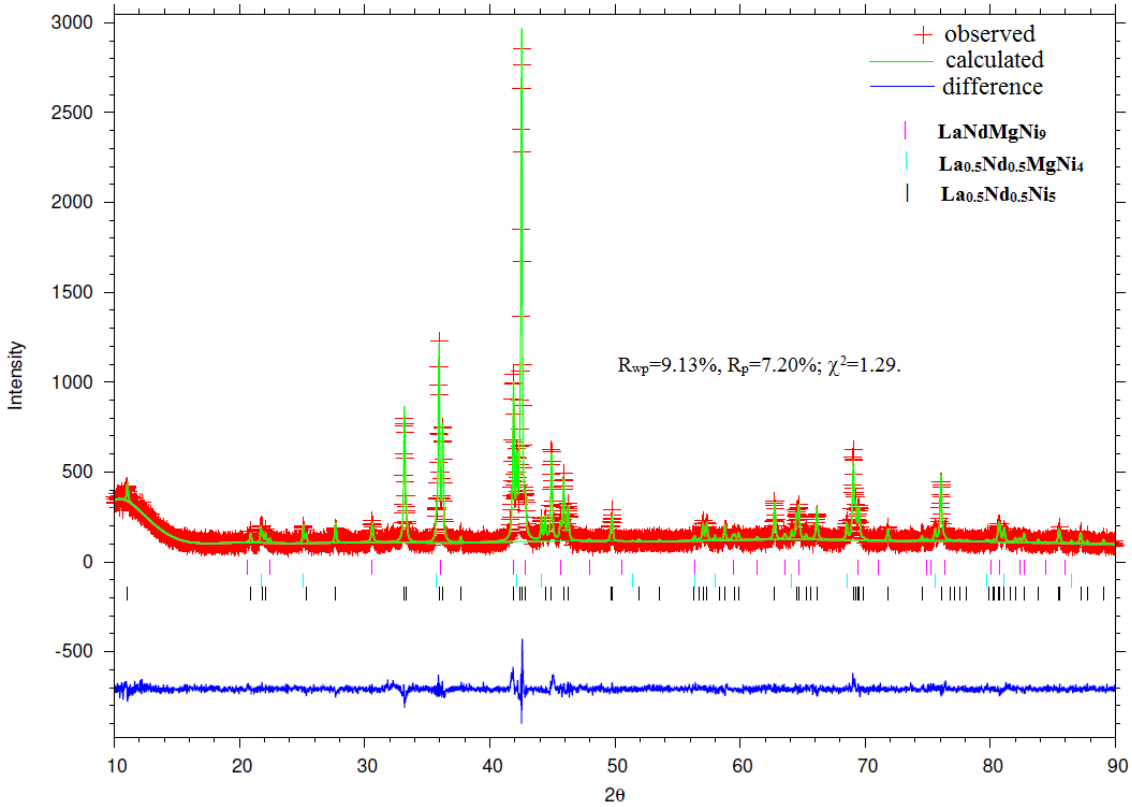

Figure S1. X-ray diffraction pattern of $LaNdMgNi_9$ alloy showing presence of $LaNdMgNi_9$ (88.0(1) %) as the main phase constituent, together with the secondary phases $La_{0.5}Nd_{0.5}MgNi_4$ (6.4(2) %) and $La_{0.5}Nd_{0.5}Ni_5$ (5.6(2)%).

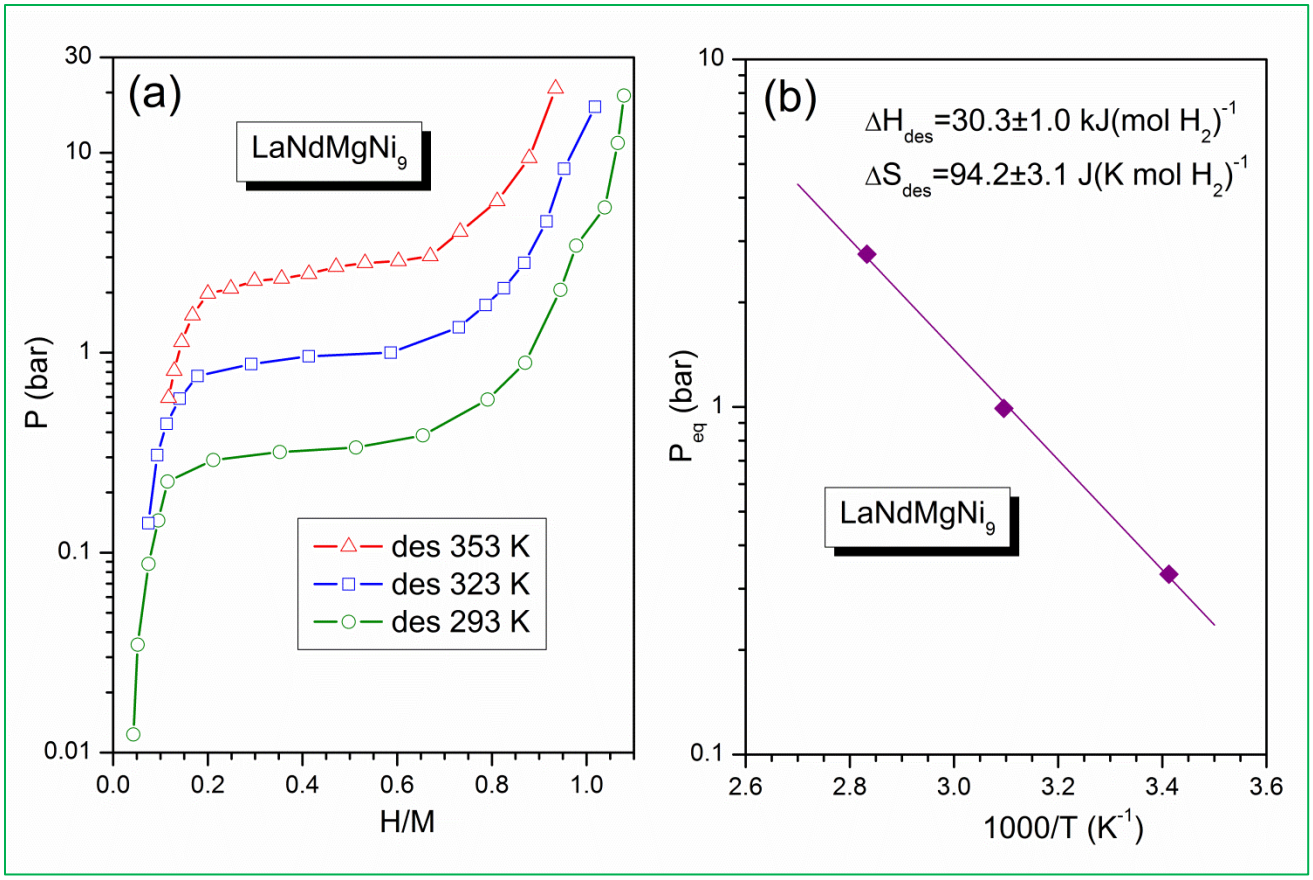

Figure S2: *PCT* diagrams (a) and van't Hoff plots (b) for $LaNdMgNi_9$–H_2 system.

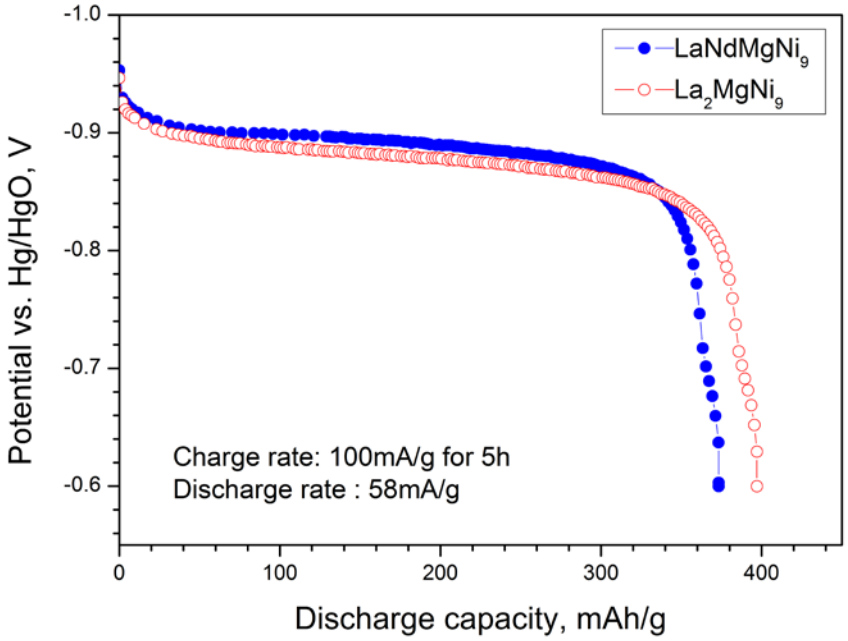

Figure S3. Galvanostatic discharge curves of the $LaNdMgNi_9$ and La_2MgNi_9 electrodes at 1/6 *C* rate.

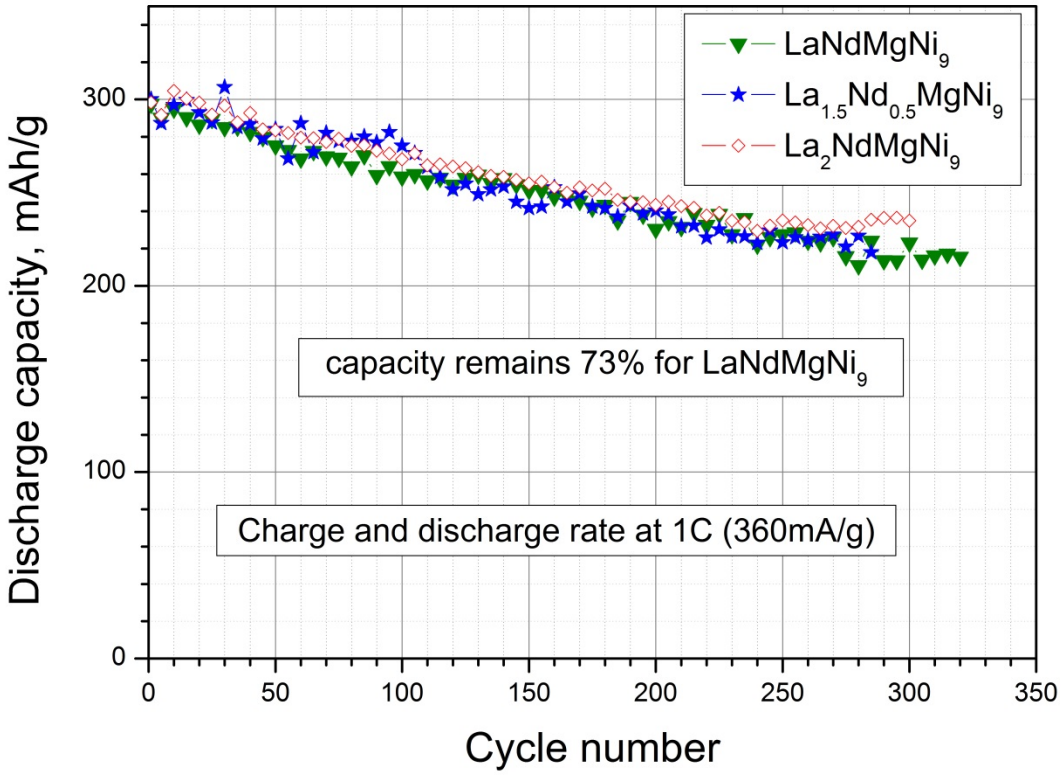

Figure S4. Cyclic stability comparison of $LaNdMgNi_9$, $La_{1.5}Nd_{0.5}MgNi_9$ and La_2MgNi_9 electrodes at a discharge current rate of *C*.

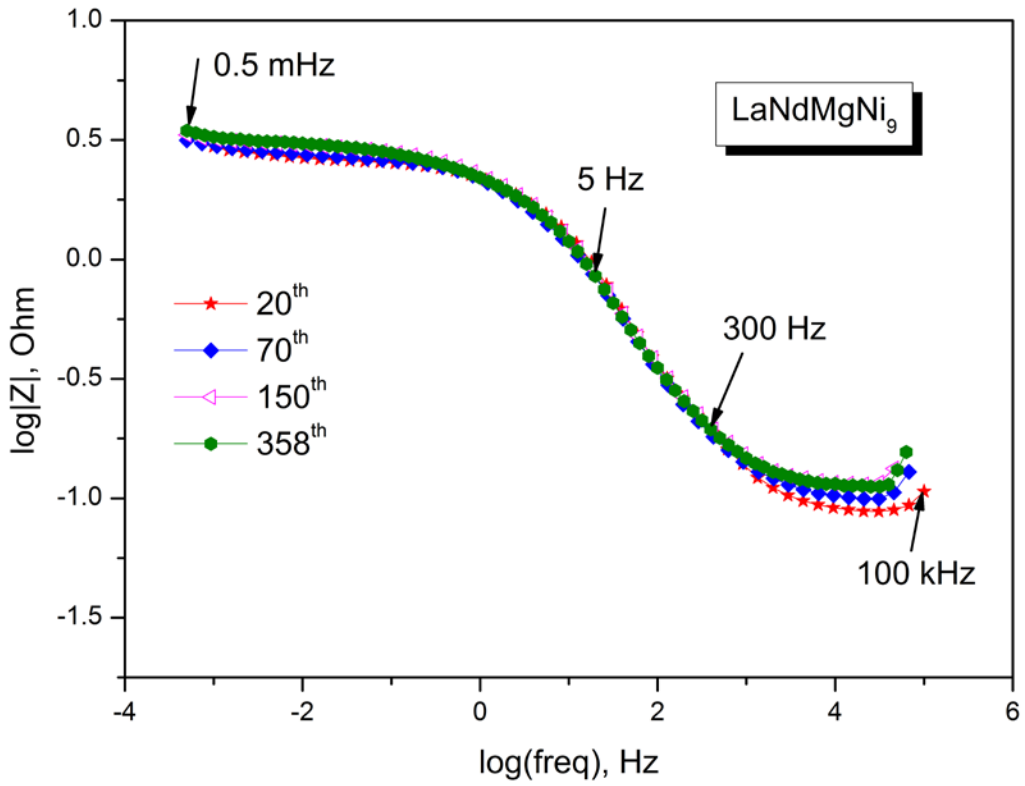

Figure S5. Magnitude Bode plots of the $LaNdMgNi_9$ electrode during galvanostatic cycling.

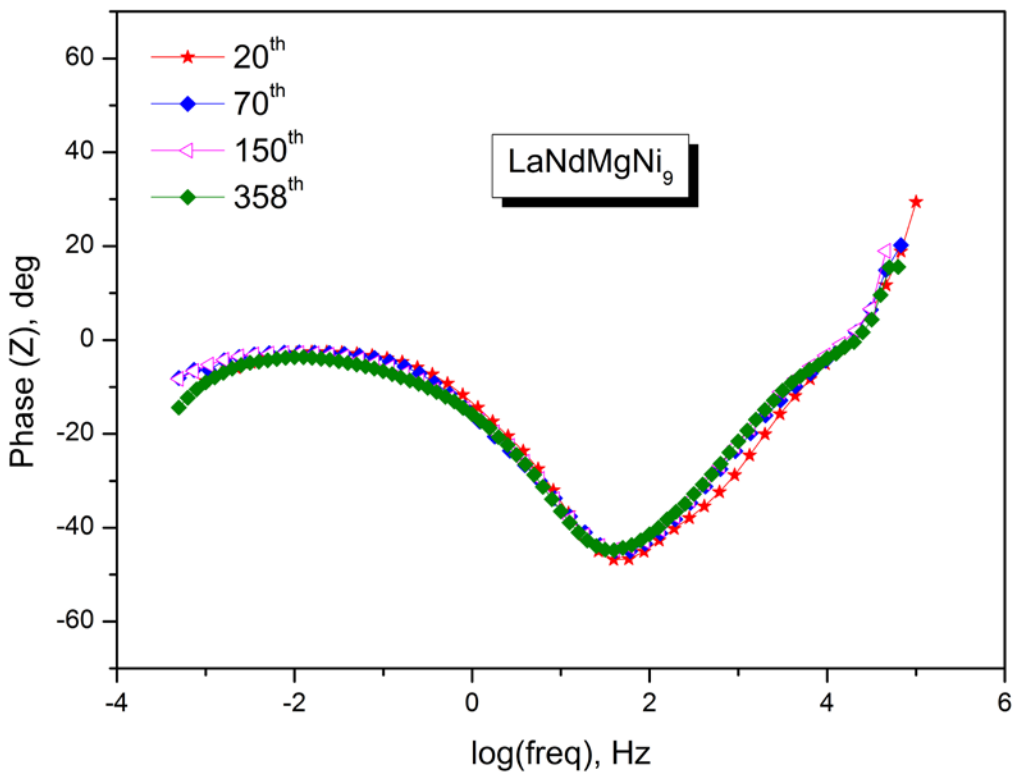

Figure S6. Angle Bode plots of the $LaNdMgNi_9$ electrode during galvanostatic cycling.

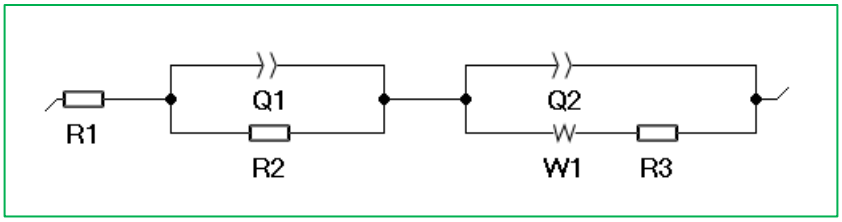

Figure S7. Equivalent circuit fitted to the EIS

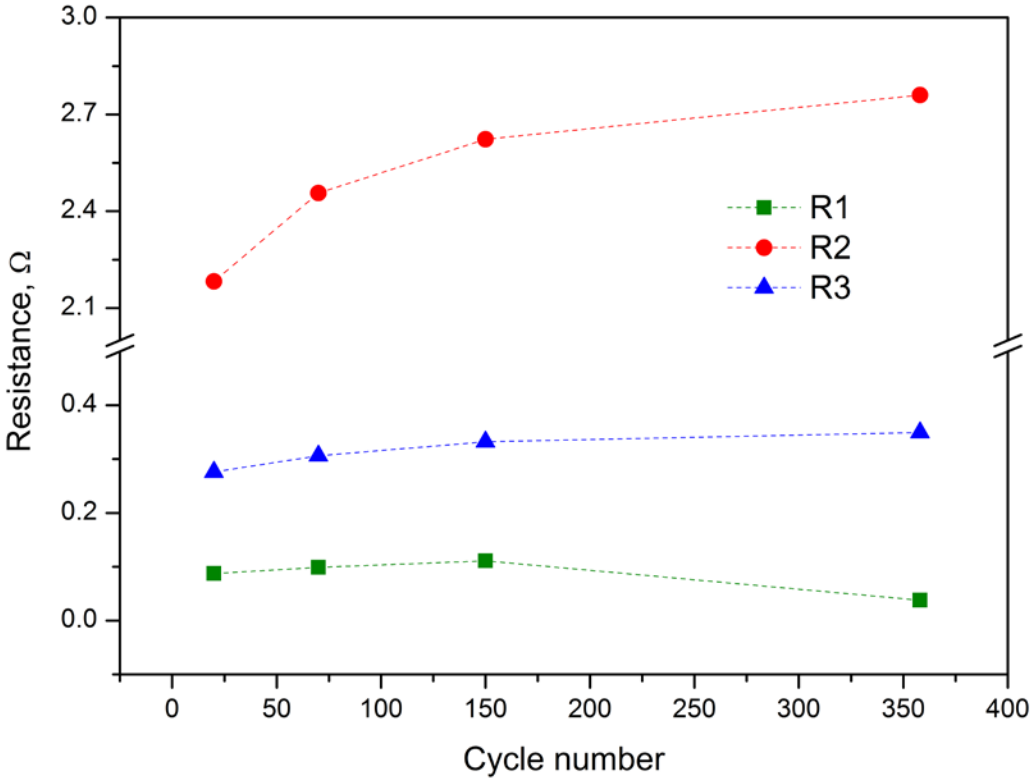

Figure S8. Resistances *R*1, *R*2, and *R*3 for the $LaNdMgNi_9$ electrode as related to the number of cycles of charge-discharge.

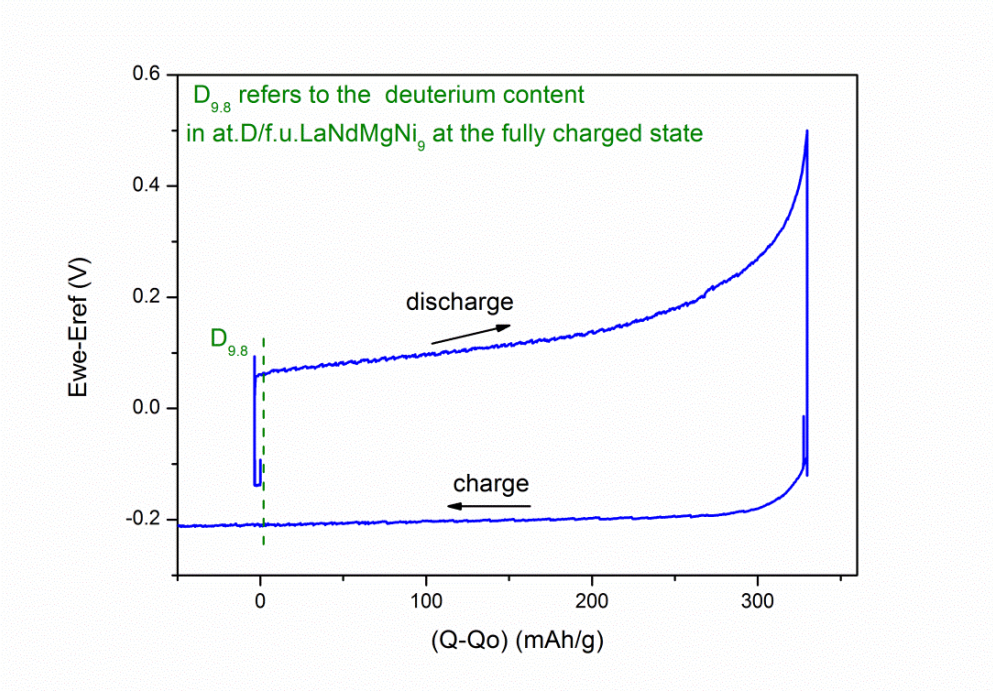

Figure S9. Potential - capacity dependence for the $LaNdMgNi_9$ electrode during in-situ galvanostatic cycling.

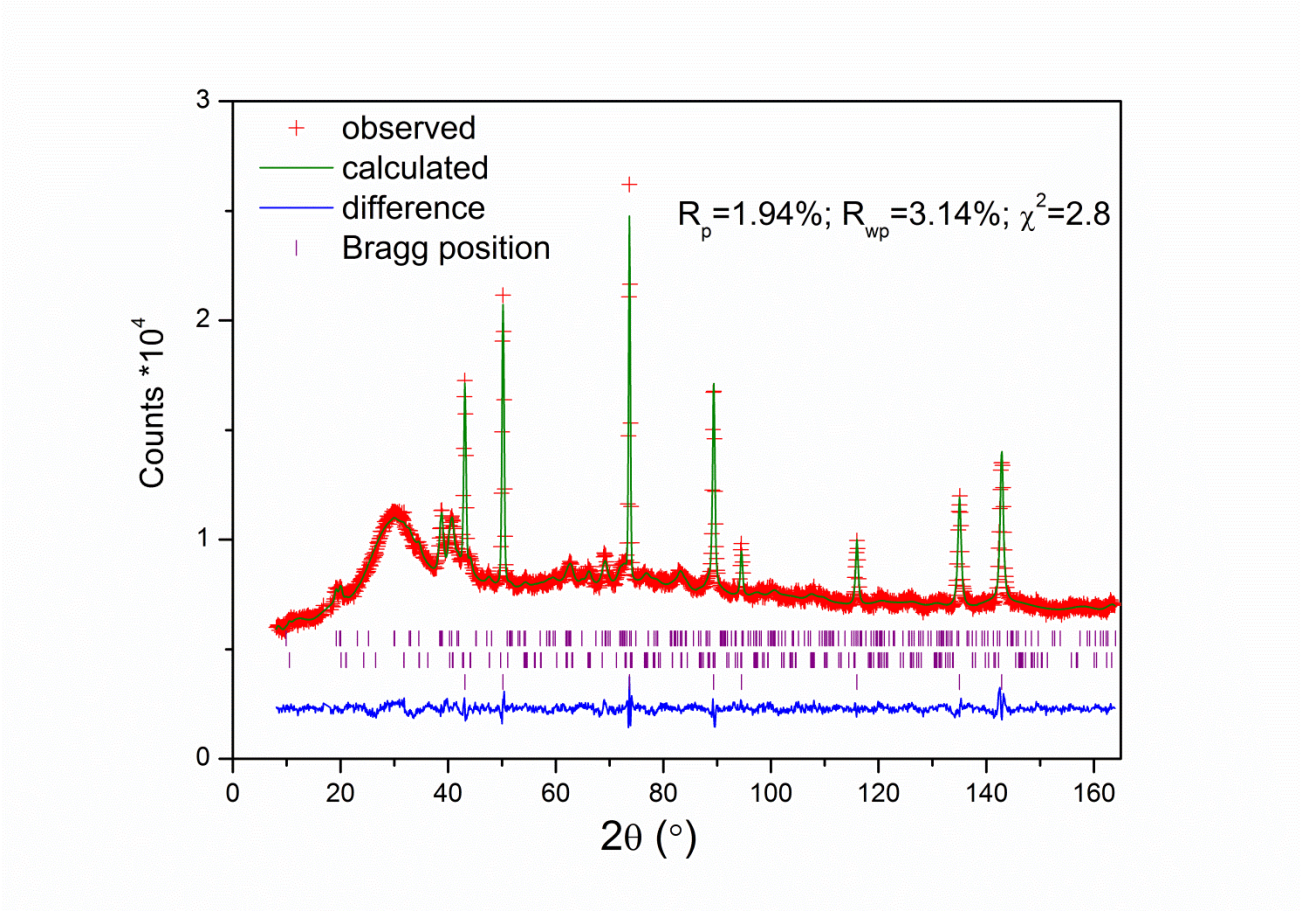

Figure S10. Refined NPD pattern of the half- discharged electrode. Phases (from top to bottom) are: $LaNdMgNi_9D_{8.2}$ (53.65 wt. %), $LaNdMgNi_9D_{1.6}$ (46.35 wt. %) and Ni. Crystallographic data are taken from [1]. Note that in the electrochemically charged electrode, the contribution from the minority secondary phases, $La_{0.5}Nd_{0.5}MgNi_4D_x$ and $La_{0.5}Nd_{0.5}Ni_5$, was marginal; thus, these phases were not introduced into the refinements.

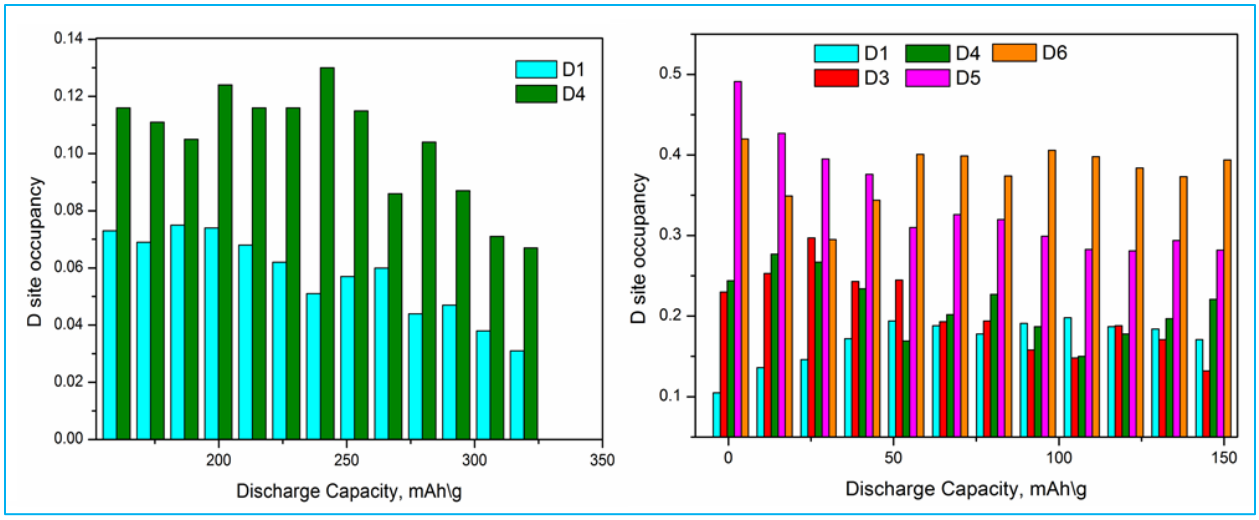

Figure S11. D site occupancies in at. D/f.u. as related to the discharge capacity for the α phase (left) and β phase (right).

Table S1.

Crystallographic data for $LaNdMgNi_9D_{1.6}$ from Rietveld refinements of *in situ* NPD data.

Space group $R\bar{3}m$; a = 5.032(3), c = 24.56(4) Å, V = 538.7(5) Å^3.

Atom	Wyckoff site	x/a	y/b	z/c	$U_{iso}\times100$ (Å^2)	Occupancy
(La/Nd)1	3*a*	0	0	0	0.01	0.5/0.5(–)
(La/Nd)2/ Mg	6*c*	0	0	0.1434	0.01	(0.25/0.25)/0.5(–)
Ni1	3*b*	0	0	½	0.01	1.0(–)
Ni2	6*c*	0	0	0.3323	0.01	1.0(–)
Ni3	18*h*	½	½	0.0835	0.01	1.0(–)
D1	36*i*	0.5754	0.5770	0.0206	0.02	0.07(2)
D4	18*h*	0.8598	0.1402	0.0748	= U_{iso}(D1)	0.12(3)

Table S2.

Crystallographic data for $LaNdMgNi_9D_{8.2}$ from Rietveld refinement of *in situ* NPD data. Space group $R\bar{3}m$; a = 5.267(2) Å, c = 26.04(2) Å, V = 625.7(4) Å^3.

Atom	Wyckoff site	x/a	y/b	z/c	$U_{iso}\times100$ (Å^2)	Occupancy
(La/Nd)1	3*a*	0	0	0	0.01	0.5/0.5(–)
(La/Nd)2/Mg	6*c*	0	0	0.1408	0.02	(0.25/0.25)/0.5(–)
Ni1	3*b*	0	0	½	0.01	1.0(–)
Ni2	6*c*	0	0	0.3285	0.01	1.0(–)
Ni3	18*h*	0.498	0.502	0.0834	0.01	1.0(–)
D1	36*i*	0.538	0.544	0.0166	0.023	0.17
D3	18*h*	0.182	0.818	0.0702	= U_{iso}(D1)	0.13
D4	18*h*	0.848	0.152	0.0704	= U_{iso}(D1)	0.22
D5	18*h*	0.496	0.504	0.1483	= U_{iso}(D1)	0.28
D6	18*h*	0.829	0.171	0.0989	= U_{iso}(D1)	0.39

Table S3.

D site occupancy comparison of different deuterated phases of $LaNdMgNi_9D_x$

$LaNdMgNi_9D_{12.9}$ (β-charged by deuterium gas)	**$LaNdMgNi_9D_{9.8}$ (β-electrochemically charged)**	**$LaNdMgNi_9D_{1.2}$ (α-discharged phase)**
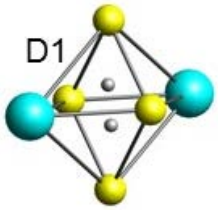	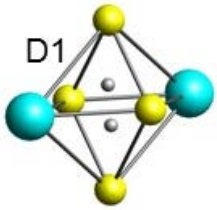	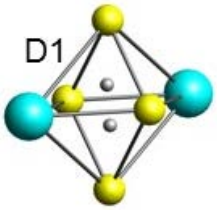
	vacant	vacant
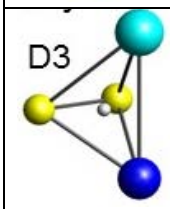	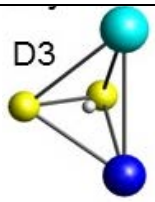	vacant
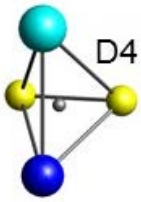	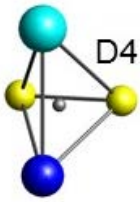	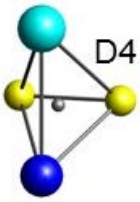
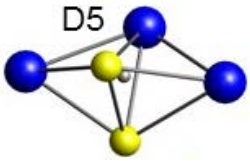	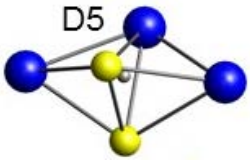	vacant
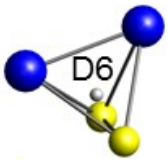	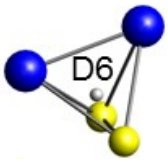	vacant
	vacant	vacant

REFERENCES

[1] Volodymyr Yartys, R. Denys, Chem. Met. Alloys 7 (2014) 1-8.